Toward Improving Ice Water Content and Snow-Rate Retrievals from Radars. Part I: X and W Bands, Emphasizing *CloudSat*

ANDREW J. HEYMSFIELD

National Center for Atmospheric Research, Boulder, Colorado*

SERGEY Y. MATROSOV

Cooperative Institute for Research in Environmental Sciences, University of Colorado, and NOAA/Earth System Research Laboratory, Boulder, Colorado

NORMAN B. WOOD

Cooperative Institute for Meteorological Satellite Studies, University of Wisconsin–Madison, Madison, Wisconsin

(Manuscript received 13 October 2015, in final form 23 March 2016)

ABSTRACT

Microphysical data and radar reflectivities (Z_e, $-15 < Z_e < 10$ dB) measured from flights during the NASA Tropical Clouds, Convection, Chemistry and Climate field program are used to relate Z_e at X and W band to measured ice water content (IWC). Because nearly collocated Z_e and IWC were each directly measured, Z_e–IWC relationships could be developed directly. Using the particle size distributions and ice particle masses evaluated based on the direct IWC measurements, reflectivity–snowfall rate (Z_e–S) relationships were also derived. For $-15 < Z_e < 10$ dB, the relationships herein yield larger IWC and S than given by the retrievals and earlier relationships. The sensitivity of radar reflectivity to particle size distribution and size-dependent mass, shape, and orientation introduces significant uncertainties in retrieved quantities since these factors vary substantially globally. To partially circumvent these uncertainties, a W-band Z_e–S relationship is developed by relating four years of global *CloudSat* reflectivity observations measured immediately above the melting layer to retrieved rain rates at the base of the melting layer. The supporting assumptions are that the water mass flux is constant through the melting layer, that the air temperature is nearly 0°C, and that the retrieved rain rates are well constrained. Where $Z_e > 10$ dB, this Z_e–S relationship conforms well to earlier relationships, but for $Z_e < 10$ dB it yields higher IWC and S. Because not all retrieval algorithms estimate either or both IWC and S, the authors use a large aircraft-derived dataset to relate IWC and S. The IWC can then be estimated from S and vice versa.

1. Introduction

Radar is an effective tool for remotely measuring the properties of snow precipitation. Directly relating a radar measurable cloud property, such as the equivalent radar reflectivity factor (Z_e), to the snow precipitation rate (S) can be used to monitor and estimate the development of snow precipitation. With the ability to map out snow precipitation globally using W-band (94 GHz), Ku-band (13 GHz), and Ka-band (35 GHz) radar measurements from *CloudSat*, the Global Precipitation Measurement (GPM), and the forthcoming Earth Clouds, Aerosols and Radiation Explorer (EarthCARE) satellites, a much better characterization of Earth's water budget is now possible.

The Z_e–S relationships developed to date are usually of the form $Z_e = AS^P$, where A is a coefficient and P the power; most relationships to date are independent of the air temperature and are applicable typically to snowfall at the surface. The relationships are developed using two basic approaches. In the first approach, radar reflectivities measured by a ground-based radar are related to coincident snowfall rates measured with precipitation gauges (Puhakka 1975; Boucher and Wieler 1985; Fujiyoshi et al.

* The National Center for Atmospheric Research is sponsored by the National Science Foundation.

Corresponding author address: Andrew Heymsfield, NCAR, 3450 Mitchell Lane, Boulder, CO 80301.
E-mail: heyms1@ucar.edu

DOI: 10.1175/JAMC-D-15-0290.1

1990), or, more recently, to a Hotplate (Wolfe and Snider 2012). To compensate for marked differences in sample volumes between instruments and for collocation errors, these studies use averaging times from 5 min to 1 h. A modification of this technique, using collocated radar and precipitation gauge data, differs in that it derives a value of A for each 30–60-min period, with the assumption that $P = 1.6$ (Rasmussen et al. 2003). The resulting relationship is used to nowcast snowfall rates. The second approach derives Z_e–S relationships based on particle size distributions (PSDs), which are either measured or, more commonly, taken from data reported in the literature, together with assumed or observed ice particle shapes, or habits (Imai et al. 1955; Sekhon and Srivastava 1970; Ohtake 1970). By default, studies using ground-based gauge observations involve systems capable of producing precipitation at the surface, while aircraft-based studies are freed from this restriction. The backscatter cross sections of the ice hydrometeors are derived and then the value of Z_e can be derived. Because non-Rayleigh scattering becomes significant when large ice particles are measured with Ku- through W-band radars, researchers have developed methods to determine the backscatter cross sections of the ice particles using T-matrix and discrete dipole approximations (Matrosov 2007, hereinafter M07; Liu 2008; Matrosov et al. 2009; Kulie and Bennartz 2009; Hiley et al. 2011; among others). Calculating backscatter cross sections is especially challenging at the W band (94 GHz), the frequency of *CloudSat* (Hong 2007; Liu 2008; Kulie and Bennartz 2009; Kulie et al. 2010; Wood et al. 2015). The cross sections depend on ice particle shape to varying degrees, depending on particle size, ice bulk density, and radar wavelength, making it necessary to model ranges of particle shapes, and the shape effects can contribute significant uncertainty to derived Z_e–S relationships. Recent studies with complex models (e.g., Petty and Huang 2010; Tyynela et al. 2011; Leinonen et al. 2012; Hogan and Westbrook 2014) indicated that for larger cloud ice and snow-sized particles, the use of shape models with homogeneous mixtures of ice and air (e.g., a soft spheroidal model) can result in significant underestimation of backscattering cross sections. The model backscatter differences are more pronounced for particles with larger size–wavelength ratios and thus are more acute for W-band frequencies. For many observed particle size distributions, however, larger particles contribute to integral backscatter relatively little because of their low concentrations and bulk densities. As a result, the homogeneous spheroidal model backscatter for particle populations is often in reasonable agreement with the range predicted by more sophisticated particle shapes (e.g., Liu 2008; Hogan and Westbrook 2014). However, the limitations of the spheroidal model can contribute to the uncertainties of modeled uncertainties of modeled W-band backscatter, especially for larger particles (higher reflectivities).

Dual-wavelength radar (DWR) techniques have shown promise in accurately estimating snowfall rates when scattering is in the Rayleigh regime at one radar wavelength and non-Rayleigh at the other (Matrosov 1992, 1998). The logarithmic difference between reflectivities at the two wavelengths provides an independent estimate of snowflake median volume size. In those articles, it is shown that the advantage of the DWR approach over the single radar Z_e–S approach is that the DWR exhibits a low sensitivity to snowflake density and details of the size distribution. While we acknowledge this method, it is not used here because it has a higher detection threshold of the X- versus W-band radar, which would reduce our sample size.

Developing algorithms to retrieve the ice water content (IWC) from radar reflectivity is also problematic. Instruments for measuring the (bulk) IWC are not readily available, and they are rarely deployed at the ground. Most determinations of Z_e–IWC relationships rely on the second approach identified above, and some further account for cloud temperature (Hogan et al. 2006; Protat et al. 2007). Other techniques replace calculated reflectivities with values measured by radar and collocated with in situ aircraft observations from which IWC can be derived (Heymsfield and Palmer 1986; Heymsfield et al. 2005). Yet other approaches relate observed reflectivities to the IWC values retrieved using multisensor observations, which are expected to be more robust than radar-only algorithms (e.g., Matrosov 1997). These implementations may use radars and infrared radiometers together (Matrosov et al. 1994), radars together with lidars (Intrieri et al. 1993; Wang and Sassen 2002; Tinel et al. 2005), and dual- or triple-wavelength radar (Sekelsky et al. 1999; Gaussiat et al. 2003). Most of these studies considered a wide range of Z_e and IWC, spanning several orders of magnitude, and were primarily oriented toward nonprecipitating clouds.

In Part I of our study, we use approaches for deriving the snowfall rate and ice water content from radar reflectivity at X (9.6 GHz) and W bands that differ from those described above. Future work will use similar approaches, focusing on Ku and Ka bands. Although we will use observations from only one location, and these are used to point out potential uncertainties in earlier relationships and in retrievals from spaceborne active remote sensors, the goal of this study is to develop a methodology and relationships that might apply more broadly. Initially, we present a method to mitigate the uncertainties involved in deriving the backscatter cross sections of the ice particles, especially for W band. These cross sections are potentially a significant source of

error in the estimated value of Z_e since they are derived by assuming ice particle shape and by using complex scattering models that are yet somewhat unvalidated by observations. Furthermore, both the PSDs (owing to their temperature dependence as well as their dependence on the relative height within a cloud) and, especially important, the particle masses used in deriving IWC, S, and Z_e are potential sources of significant error. In this study, we directly relate the IWC measured in situ by an aircraft instrument to the Z_e measured at X and W bands by an aircraft overflying the in situ aircraft. Given the direct IWC measurements, together with detailed ice particle imagery, we can more reliably develop Z_e–S relationships. We also derive IWC and S from the measured PSDs. Our results are compared with previously developed relationships and with *CloudSat* retrievals from almost five years of near-global observations. To develop more globally relevant relationships, we compare estimates of rain rate R derived from *CloudSat* retrievals of rainwater content just below the melting layer with the W-band reflectivities just above the melting layer. With the assumption that the precipitation rate across the melting layer is approximately constant, we can then relate R to Z_e to develop a Z_e–S relationship in a different way. Finally, we relate the IWC from direct measurements encompassing a large body of in situ data from many locations to the S calculated from the measured PSDs and ice particle imagery. Because IWC has fewer variables in its calculation than does S, some of the earlier Z_e–IWC relationships can then be used to derive S; or, conversely, the directly measured snowfall rate from Z_e–S relationships could potentially be used to derive the IWC.

In section 2, we discuss the data sources. In section 3, we present the in situ measurements of IWC and S collocated with the Z_e measured from the overflying aircraft and relate our results to those from earlier studies and from the most recent retrievals using *CloudSat* W-band measurements. In section 4, we discuss several possible sources of differences between our relationships and those derived earlier. The results are summarized and discussed further in section 5.

2. Data

This section presents the datasets that are used in the development of Z_e–S and Z_e–IWC relationships.

a. DC-8 in situ data

The Tropical Clouds, Convection, Chemistry and Climate (TC4) field program was based in Costa Rica in 2007 (see Toon et al. 2010). During this experiment, the ER-2 aircraft, with X- and W-band radars (Heymsfield et al. 2010) and a cloud lidar (McGill et al. 2003), flew coordinated tracks with the NASA DC-8 aircraft, which was equipped with a set of microphysical probes. Flights on three days were available for this study: 22 and 31 July and 8 August. Sampling temperatures ranged from about −19° to −52°C, and the clouds were all stratiform ice clouds/anvils, not producing precipitation at the surface and formed from the outflow of thunderstorms (see Fig. 1). The total condensed (liquid + ice) water content was measured by a counterflow virtual impactor probe (CVI; Twohy et al. 1997).

Particle probe measurements from the DC-8 were made with a combination of a Droplet Measurement Technology (DMT) cloud imaging probe (CIP), sizing from about 50 to >1500 μm, and a DMT-modified precipitation imaging probe (PIP), sizing from about 200 μm to 6 mm, with "reconstruction" of partial images allowing particles >1 cm in diameter to be sized and concentrations measured (Heymsfield and Parrish 1978). Most artifacts produced from shattering of ice on the inlets of the particle probes have been removed objectively, using particle interarrival times (Field et al. 2006). More details of the TC4 particle probe data are given in Heymsfield et al. (2013). A DMT cloud aerosol spectrometer (CAS) sized in the range from about 1 to 30 μm. These data were used only to identify liquid water regions where CAS concentrations were higher than 5 cm^{-3}; those regions are excluded from this analysis.

To calculate the IWC, ice particle masses (m) were estimated from a power-law relationship,

$$m = aD^b, \tag{1}$$

where $a = 0.0052$ and $b = 2.1$ (cgs units), based on a large dataset of CVI measurements in a wide range of ice clouds (Heymsfield et al. 2013). In Eq. (1) and hereinafter, D is the maximum physical dimension of a particle as found from the particle image as the minimum diameter of a circle that fully encloses the particle.

The S was also calculated using this $m(D)$ relationship. Snowfall rate is proportional to the integral over PSD of the product of the mass and terminal velocity (V_t). Mass was derived as above, and V_t was derived from this mass and the particle cross-sectional areas measured by the imaging probes (Heymsfield and Westbrook 2010). Other $m(D)$ relationships are also used in order to examine the sensitivity of IWC and S to the choice of the $m(D)$ relationship, as described in section 3b.

b. ER-2 radar data

Radar reflectivities during TC4 were measured from two radars on board the NASA ER-2 aircraft: the ER-2 X-band Doppler radar (EDOP) and a W-band Doppler

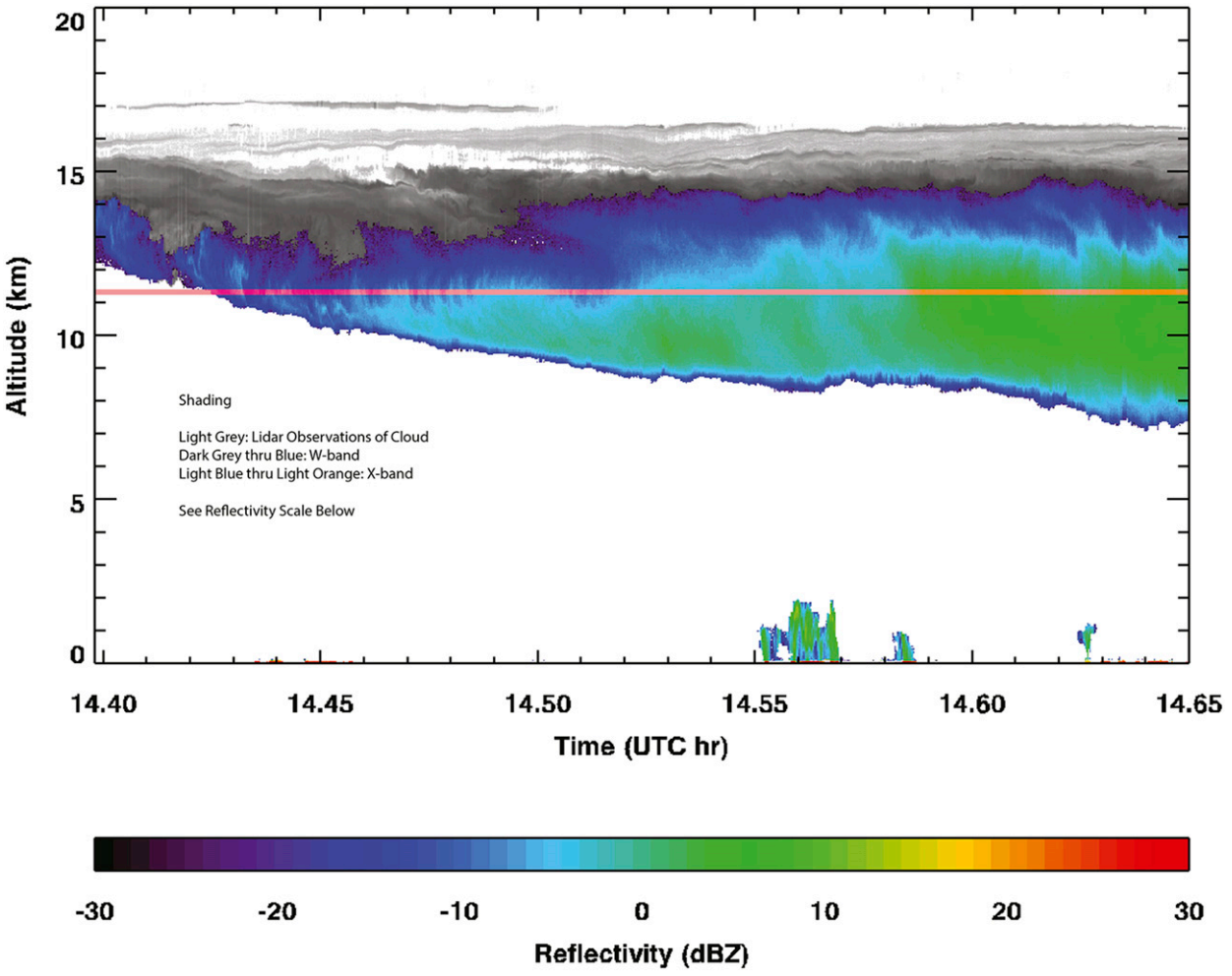

FIG. 1. Composite of NASA ER-2 lidar [cloud physics lidar (CPL); thin lines above 15 km], W-band radar (CRS), and X-band radar measurements on 31 Jul 2006, during an overflight of the DC-8 aircraft (horizontal line between 11 and 12 km) for the period 1504–1530 UTC.

radar, the Cloud Radar System (CRS; Heymsfield et al. 2010). The reflectivity data have been calibrated to within about 1 dB by internal and external calibrations and checked against the ocean surface return (Heymsfield et al. 2010). For the TC4 data, further cross calibration of the two radars near the tops of ice clouds indicates a difference of less than 0.5 dB. Thus, the absolute error of each radar is $\sim\pm1$ dB.

c. *Collocations of DC-8 and ER-2*

We use collocations between the ER-2 and the DC-8 aircraft to relate the in situ and remote sensing observations. Arbitrarily, we define a ''collocation'' to occur in the following way. For each 1 s of a DC-8 time, a circle of 3-km diameter is drawn, centered on the location of that 1-s period. If the ER-2 flies within one of the circles within ±10 min of that time, a ''collocation time'' is designated. There were a total of 2700+ 1-s in-cloud collocations on 22 July, 3300+ 1-s collocations on 31 July, and 5400+ collocations on 8 August. We have halved the separation time to 5 min, and this made little difference in the relationships we derived but it led to significantly fewer points, larger standard deviation, and the need to widen the ice water content and reflectivity averaging bins. Ensuring that the data from all altitudes were above the radar-detection thresholds, the minimum detectable reflectivity of the X-band radar (-5 dBZ at a range of about 13 km, or a height of about 5 km MSL) versus that of the W band (-15 dBZ) resulted in far fewer collocation points at X band than W band.

d. CloudSat *data*

We compare our results with those derived from global distributions of snow and ice cloud properties derived

from the *CloudSat* W-band radar. *CloudSat* ice water content and snowfall-rate retrievals were obtained from release R04, using observations from epoch 1, starting 7 July 2006, through epoch 4, ending 17 April 2011. We use the *CloudSat* 2C-Snow Water Content and Snowfall Rate (2C-SNOW-PROFILE, hereinafter 2C-SNOW), which uses a Bayesian retrieval algorithm implemented with optimal estimation (Rodgers 2000), estimating the observed state using the measurements in conjunction with an explicit a priori estimate of the state. These are applied to vertical profiles of W-band radar reflectivity observed by *CloudSat*'s Cloud Profiling Radar (CPR). A retrieval is performed when an analysis of the reflectivity profile and an associated temperature profile suggests snow is occurring at the surface. The retrieval algorithm then operates on the lowermost contiguous range of radar bins that appear to contain snow. The retrieval estimates snow PSD parameters using a priori information about snow PSDs and snow particle microphysical and radar scattering properties (Wood et al. 2015). From the a priori microphysics and the retrieved PSD parameters, the algorithm estimates vertical profiles of ice water content and snowfall rate. The terms in the $m(D)$ relationship [Eq. (1)] used in the 2C-SNOW algorithm are $a = 0.0033$ and $b = 2.25$. The 2C-SNOW snow rates are calculated using size-resolved fall speeds (Mitchell and Heymsfield 2005) that are sensitive to vertical variations in atmospheric pressure and temperature. Here, snowfall rates are derived for standard temperature and pressure conditions (273 K, 1000 hPa). Because W-band radar observations can be affected by attenuation and multiple scattering, the radar reflectivity factors in the data used here were synthesized using the algorithm's assumed scattering properties and the retrieved size distributions to calculate the singly scattered, unattenuated radar reflectivities.

Ice water contents were also obtained for the same periods using the *CloudSat* 2C-ICE product (Deng et al. 2013). By combining *CloudSat* reflectivities and *CALIPSO* lidar backscatter data, the 2C-ICE method provides a vertically resolved retrieval of ice cloud properties, such as the effective radius, IWC, and visible extinction. The product is primarily aimed at upper-tropospheric ice clouds ranging from optically thin cirrus to optically thicker anvils (Deng et al. 2010).

3. Results

This section develops ice water content–radar relationships at X and W bands using direct measurements of the radar reflectivity and the IWC for the ER-2–DC-8 collocation times from the TC4 field program. Also developed are Z_e–IWC and Z_e–S relationships using the measured PSDs and the $m(D)$ relationship with $a = 0.0052$ and $b = 2.1$ as described earlier; The terminal velocities (V_t) are calculated as described above, with the assumption that the atmospheric pressure is 1000 hPa to allow for consistent comparisons with surface-based observations. Further, Z_e for the two radar frequencies X (9.6 GHz) and W band (94 GHz) are derived using the observed PSDs, the $m(D)$ relationship, and backscatter cross sections from the standard Mie-spheres approximation (Bohren and Huffman 1983) and the T-matrix backscatter coefficients of M07, assuming that the particles are oblate spheroids with an aspect ratio (minor to major dimension) of 0.6, which follows from the study of Hanesch (1999) and Korolev and Isaac (2003). The bulk density of the particles was calculated as the ratio of their mass to the spheroidal volume. From the distributions of the IWC and radar reflectivity contributions with size, the median mass- and reflectivity-weighted particle sizes, D_m and D_Z, respectively, are also derived. In the figures that follow, standard deviations are shown except where they add too much clutter.

a. Overview of the data from individual flights

In this section, we present an overview of the measurements and calculations for each flight, focusing on one $m(D)$ relationship (from Heymsfield et al. 2013, hereinafter H2013) to illustrate some key points. Figures 2a and 2b show the distribution of the measured reflectivities with temperature at X and W band, respectively, for those periods designated as ER-2:DC-8 collocations. To select those times when the measured reflectivities are above the radar noise levels, the following criteria are used: $-5 < Z_e < 10$ dBZ (the upper limit measured) for EDOP, and $-15 < Z_e < 10$ dBZ for CRS. As noted from the number of collocation times on the left side of each panel in the figure, there were many more collocation times at W band than X band. Most of the cloudy regions sampled during the collocations on 22 July were for temperatures (T) $-19 < T < -48$°C, on 31 July $-55 < T < -28$°C, and on 8 August $-50 < T < -9$°C.

1) In situ data

The correspondence between the measured (IWC_{CVI}) and PSD-derived IWC (IWC_{PSD}) is good (Figs. 3a–c). Note that there is lag in the change in the IWC_{CVI} during rapid fluctuations in the ambient value, which introduces scatter when compared with the IWC_{PSD}.

We summarize the results in the panels in this way. First, the median ratio of IWC_{CVI}/IWC_{PSD} for all points combined on 22 July was 1.25 (IWCs underestimated by IWC_{PSD}), on 31 July it was 1.12 (IWCs underestimated by IWC_{PSD}), and on 8 August it was 0.93 (IWCs overestimated by IWC_{PSD}). Second, with decreasing IWC_{CVI}

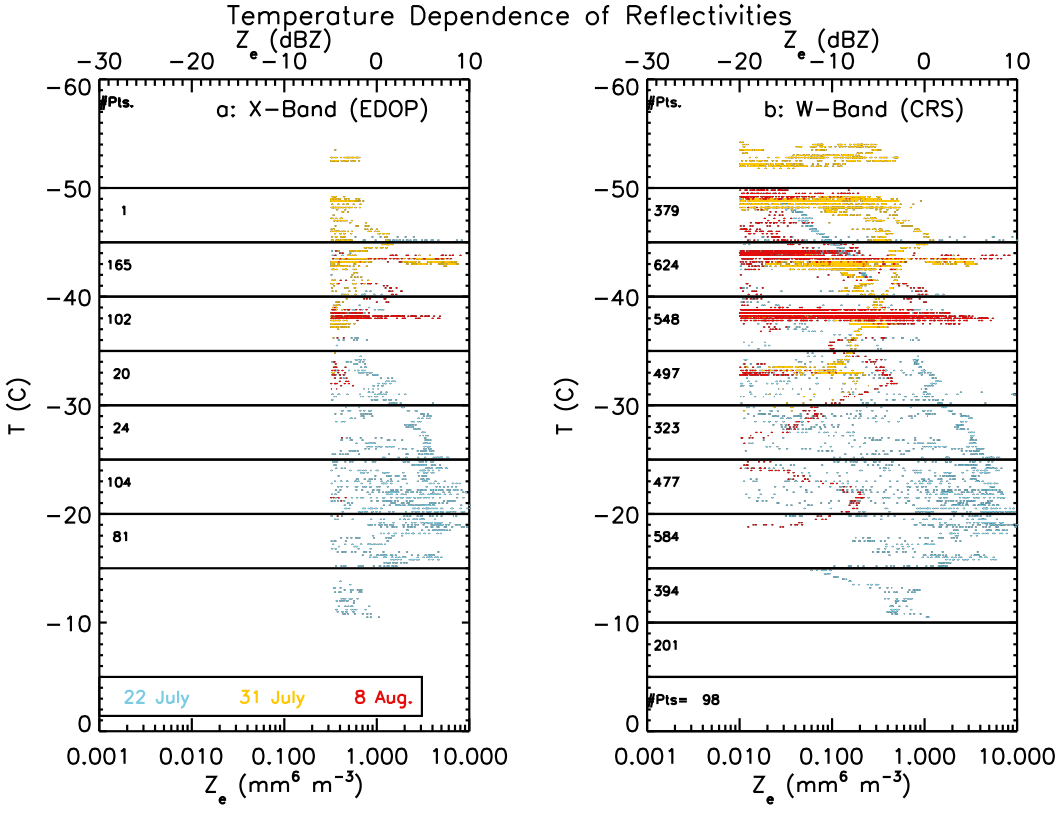

FIG. 2. Reflectivity measured from the ER-2 aircraft at (a) X band (EDOP) and (b) W band (CRS) as a function of temperature for those 1-s times identified as ER-2–DC-8 collocations for three TC4 flights. The points are color coded according to the flight date. The number of collocation times corresponding to the points are shown for 5°C temperature intervals (left side of each panel).

below 0.025 g m^{-3}, the IWC$_{PSD}$ are increasingly higher than IWC$_{CVI}$, reaching about 20% higher at 0.0125 g m^{-3}; between 0.025 and 0.08 g m^{-3}, they are quite accurate; above 0.08 g m^{-3}, the trends are case specific. Given the median values of the ratio IWC$_{CVI}$/IWC$_{PSD}$, we surmise that S derived from the PSDs will be almost as accurate as was found for the IWCs if the particle fall velocities are appropriate, since S represents a moment of the PSD that is only slightly larger than that for IWC. This point is examined later.

Figures 3d–f show the ratio of IWC$_{CVI}$/IWC$_{PSD}$ in terms of the PSD median mass size. In general, D_m increases with the IWC (not shown). For each of the cases, the values of D_m are quite flat and support the view that the results for a particular case depend upon the meteorology and do not show a systematic error in the $m(D)$ relationship with size.

2) RADAR DATA FROM OVERFLYING AIRCRAFT

The DWR derived from dBZ_{EDOP} − dBZ_{CRS}, should, in principle, be a measure of the particle characteristic size. On 22 July, the relatively low DWR values in comparison with the other two flight days (Figs. 4a–c) are presumably due to the relatively low values of characteristic size (Figs. 4d–f). Figure 4a also suggests is that the two radars have about the same calibration because the DWR at the lower reflectivities are generally between 0 and 1 dB.

3) CALCULATIONS FROM THE IN SITU DATA AND COMPARISONS WITH THE MEASUREMENTS

A comparison of the radar reflectivities measured by the ER-2 X- and W-band radars with those calculated from the PSDs using the Mie-sphere and the T-matrix approach assuming spheroidal ice particles can be used to discern some interesting aspects of the ability to accurately calculate Z_e from the PSDs. At X band, the non-Rayleigh scattering effects should be small where $Z_e < 10$ dBZ [Matrosov et al. (2009), who showed that the Rayleigh approximation is generally satisfactory at X band for particles smaller than about 5 mm]. Therefore, the measured and calculated (Z_{PSD}) reflectivities should be about the same for the collocation times, unless there are errors in the estimated ice particle masses for the sizes contributing most to Z_e. (This finding ignores the large

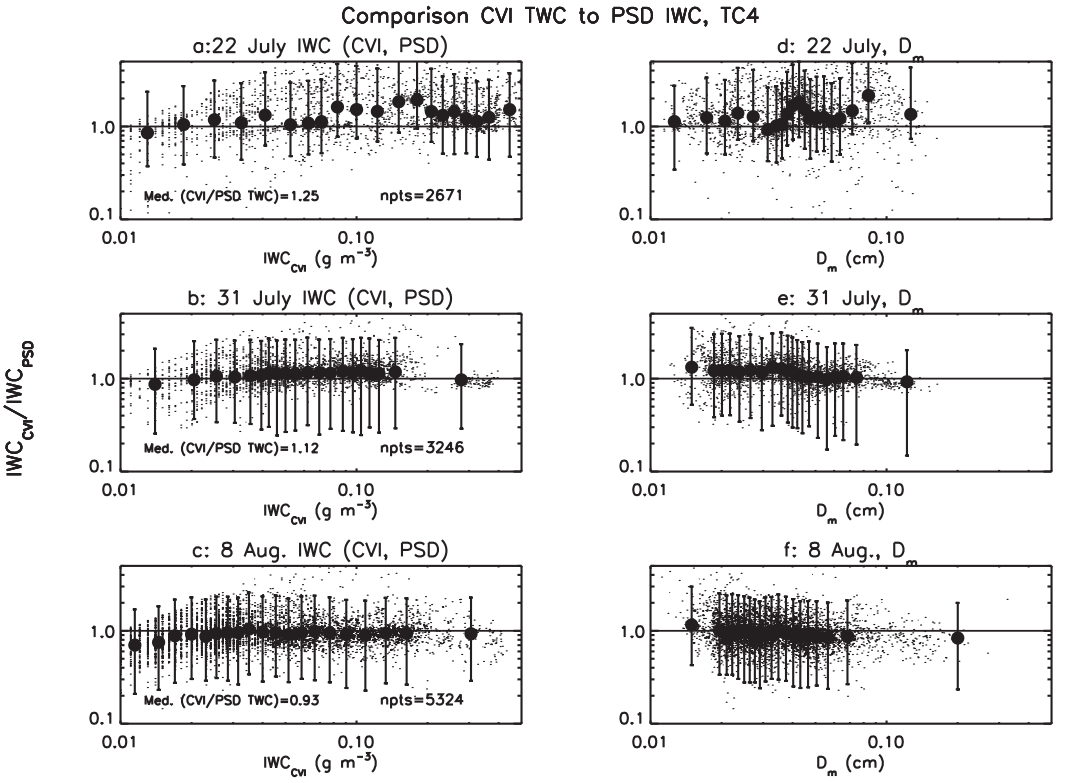

FIG. 3. (a)–(c) Ratio of the measured (CVI) to calculated (PSD) IWC as a function of the measured IWC, during the times of the collocations for the three DC-8 flights used in this study. (d)–(f) As in (a)–(c), but as a function of the median mass-weighted particle diameter. The large black circles are the median values, and the vertical lines denote the standard deviations.

mismatch between the sample volume of the radars and the particle probes and the small errors resulting from time and position differences between the DC-8 and ER-2 that we have used to define the collocations.) Another piece of information comes from the comparison of the measured and calculated IWCs (Figs. 3a–c), which suggests that for median mass diameters below about 800 μm, our estimates of the particle masses are quite accurate (Figs. 3d,e).

For the 22 July case, there are only a few dB differences between the measured and calculated reflectivity values, on average (Fig. 5a). However, the Z_e from the PSDs are larger than measured values by 4–8 dB on the other two days (Figs. 5b,c). The mass- and reflectivity-weighted mean sizes can aid in interpreting these results. The D_Z values for the 22 July case have a median value of 0.9 mm and the median ratio of D_Z/D_m is 1.46 (Fig. 5d), supporting the view that our $m(D)$ relationship is relatively accurate for sizes below about 1 mm. For the other two cases, the median D_Z values are much larger, 1.4 and 1.2 mm, and the ratios are 2.13 and 2.14. The mismatch noted between the D_Z and the D_m values (Figs. 5e,f) would suggest that too much mass is assumed for >1 mm particles.

The particle mass needed to give the X-band measured reflectivity can be estimated by using the calculated and measured values of Z_e for each collocation time. The mass change that equates to the error in the calculated radar reflectivity factor (e.g., Hammonds et al. 2014) can be evaluated from (where ~ means proportional to)

$$Z \sim m^2, \tag{2}$$

$$Z_{\text{new}}/Z_{\text{old}} \sim (m_{\text{new}}/m_{\text{old}})^2, \quad \text{and} \tag{3}$$

$$\Delta\text{dB}Z \sim 20[\log_{10}(m_{\text{new}}/m_{\text{old}})]. \tag{4}$$

In Figs. 5a–c, we have taken each value of $\Delta\text{dB}Z_e$ and calculated the corresponding ratio of $m_{\text{new}}/m_{\text{old}}$. These ratios are annotated above each D_Z value in the figure. The downward adjustments to the original assumed masses are about 0.8 for the 22 July case, and 0.4 to 0.5 for the other two cases. Combining the new masses and the corresponding D_Z for all cases, a least squares relationship was fit to yield a new $m(D)$ relationship:

$$m = 0.003\,79D^{2.21}, \tag{5}$$

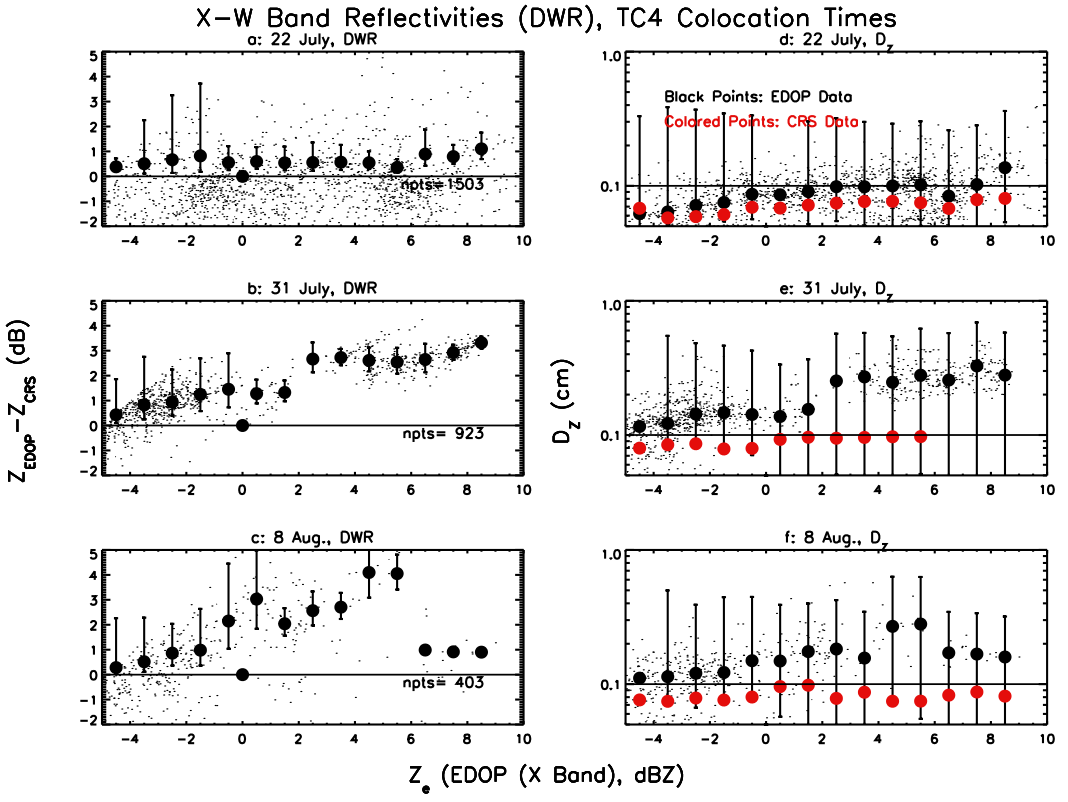

FIG. 4. (a)–(c) Dual-wavelength ratio (defined here as X-band − W-band reflectivity) for the three days, and (d)–(f) the corresponding reflectivity-weighted mean diameters at X band and W band.

quite similar to the relationship used by the *CloudSat* 2C-SNOW algorithm (section 2d). At diameters of 100 and 500 μm and 2 mm, Eq. (5) yields masses that are 0.44, 0.52, and 0.61 times the original masses. Those would fit the annotated values shown in Figs. 4d–f quite well, and they are in the correct direction to explain the differences between the measured and calculated IWCs in Fig. 3.

If the backscatter cross-section model is reliable and the W-band reflectivity measurements are accurate, then the errors at W band for $Z_e < -5$ dBZ, where non-Rayleigh scattering is likely to be minimal, should be similar to what was found at X band (see Liao et al. 2008); that is, mass errors would dominate the error. Overall, the W-band reflectivities calculated from the Mie-spheres model appear to provide a slightly better match to the CRS measurements (Fig. 6) than do those from the T-matrix spheroidal model. Thus, with adjustments to the particle mass, the spheroidal model for W band should more closely match the measurements.

b. Z_e–IWC and Z_e–S relationships for X and W band developed from combined dataset

In the following discussion of the TC4 data, we combine the data from all three cases to derive Z_e–IWC and Z_e–S relationships, and in the process we evaluate other $m(D)$ relationships in the context of the observations. Most $m(D)$ relationships take the power-law form given by Eq. (1), where from CRYSTAL-FACE convectively generated ice clouds, $a = 0.0061$ and $b = 2.05$ (Heymsfield et al. 2004, hereinafter CF); from stratiform ice cloud, $a = 0.00294$ and $b = 1.9$ (Brown and Francis 1995, hereinafter BF); and for the relationships used earlier in this section, $a = 0.0052$ and $b = 2.1$ (H2013). For convectively generated ice clouds in the central Pacific area, Heymsfield et al. (2002) developed a relationship that included the "area ratio" (A_r) of the ice particles, which they defined as the ratio of the ice particle area to the area of a circle of the same maximum diameter, as

$$m = k(A_r)^n D^\alpha, \tag{6}$$

where $k = 0.07$, $n = 1.5$, and $\alpha = -0.05$. This relationship is identified as TRMM. The relationship between the IWC calculated from the PSDs and that measured by the CVI as derived from the four $m(D)$ relationships (Eqs. 1 and 6) are shown in Fig. 7a. Where IWC < 0.1 g m^{-3}, H2013 and BF fit the measurements quite well, with CF providing overestimates by about 20% and TRMM underestimating by ~40%.

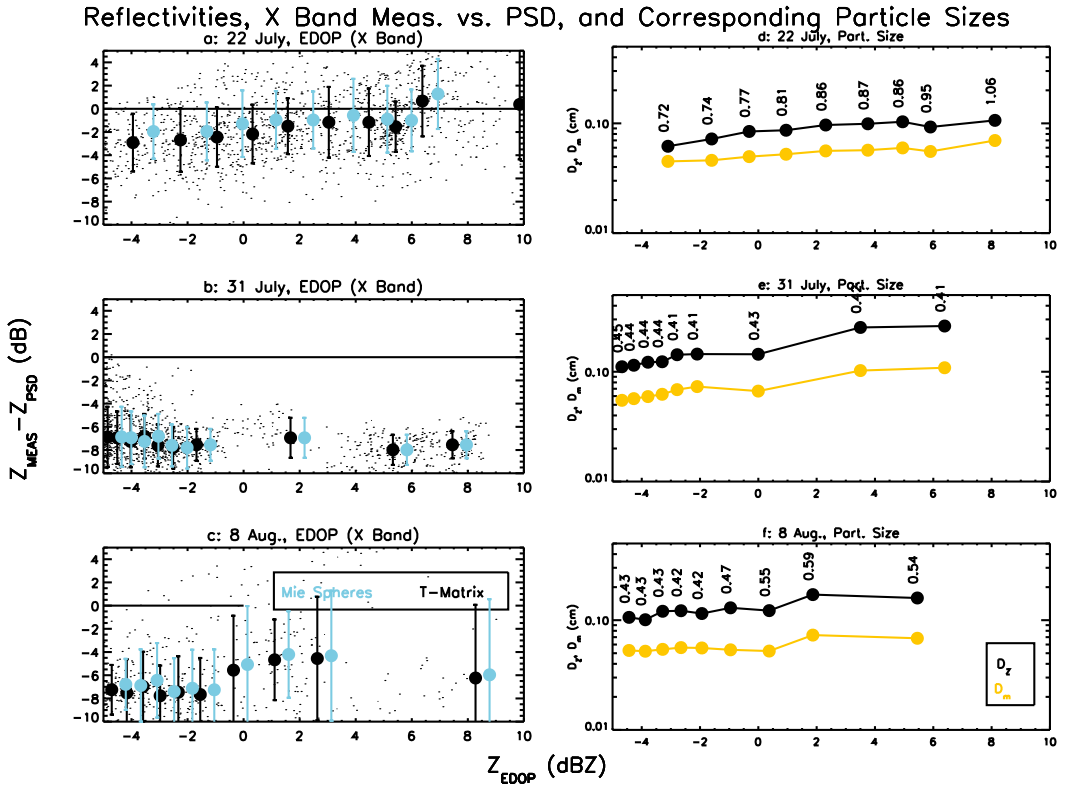

FIG. 5. (a)–(c) Difference between the radar and PSD-derived values of Z_e at X band for the three days, and (d)–(f) the corresponding reflectivity (black points) and mass-weighted (yellow points) mean diameters. In (d)–(f), numbers above the black lines show the fractional decrease in the particle mass needed for the calculated reflectivity to match the measured values.

Power-law curves of the form

$$\mathrm{IWC}_{\mathrm{CVI}} = c(\mathrm{IWC}_{\mathrm{PSD}})^{d} \tag{7}$$

are fitted using a least squares method to the relationship between the measured and calculated IWCs for each of the $m(D)$ relationships, with the associated correlation coefficients shown (Fig. 7). Each of the power-law curves has a high correlation coefficient, indicating that the fits are good. Because the correlation coefficients of the fits are high yet the exponent d in all of the fits is in the range 0.80–0.88, it is unclear what the form of the $m(D)$ relationship needs to be to provide a good match with the measured IWC across the full range of IWCs measured. It is suggested by Eq. (5) that a value of $b = 2.21$ could be a better fit to the data, but it is also possible that the difficulty in finding one relationship is because we have combined the data from all three cases. Nonetheless, it points to possible errors in the Z_e–IWC relationships developed from the use of a single $m(D)$ relationship in earlier studies.

Because there are no direct measurements of the snowfall rates to evaluate our calculations, Fig. 7b compares the snowfall rates derived from the H2013 $m(D)$ relationship with those derived from the other $m(D)$ relationships, all using the Heymsfield and Westbrook (2010) terminal velocity model. In the figure, the rates from BF fit closely to the H2013 rates, with deviations between the two of <10%. Although differences in the coefficients and exponents of the $m(D)$ relationships for BF and H2013 cause mass to be distributed differently across the particle size spectrum, the resulting snowfall rates are quite similar. The rates derived from the TRMM relationship are considerably lower and those from the CF relationship considerably higher than the H2013 approach, consistent with the findings from the IWC comparison.

A way of showing how the $m(D)$ relationships fold into the terminal velocity calculations for the same particle shapes (derived from the imaging probe data) is by deriving an ensemble mean terminal velocity (V_s) that is related to the snowfall rate. The S is the ice mass flux, given by

$$S\ (\mathrm{mm\,h^{-1}}) = [\mathrm{IWC}\ (\mathrm{g\,m^{-3}}) \times 10^{-6} V_s\ (\mathrm{cm\,s^{-1}}) \times 3600\ (\mathrm{s\,h^{-1}})]/\rho_w\ (\mathrm{g\,cm^{-3}}), \tag{8}$$

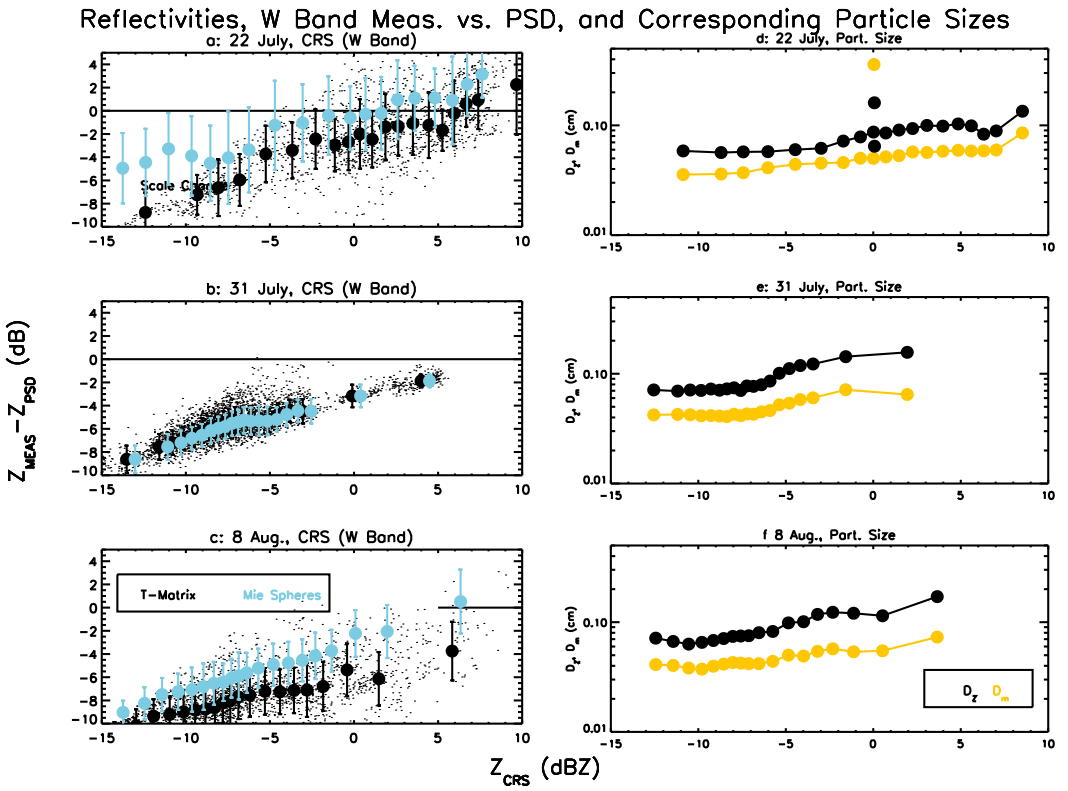

FIG. 6. As in Fig. 5, but for W band and without the annotated numbers in (d)–(f) because it is difficult to separate the effects of mass and non-Rayleigh scattering.

where ρ_w is the density of water. Solving for V_s is useful because it allows comparison with the assumptions used in the *CloudSat* snowfall-rate retrieval algorithm discussed later. Figure 8a shows the relationship between S and IWC, and the lines of constant V_s in the figure indicate that V_s increases with IWC and S. What is quite nice is that the S–IWC relationships are nearly the same for the different $m(D)$ relationships, that is, they nearly converge to the same functional form. Figure 8a does suggest, and Fig. 8b shows, that V_s does depend on the $m(D)$ relationship, exhibiting a factor of almost 2 variations in magnitude across the range of IWCs. It would be hoped that differences in the $m(D)$ relationship would affect S and IWC similarly, which would lead to nearly the same values of V_S for a given IWC, but this is not the case. Thus, the $m(D)$ relationship has a significant effect on the ice particle terminal velocities. Therefore, any errors in the $m(D)$ relationship used to calculate IWC and S from the PSDs and to determine the backscattering properties that relate them to Z_e yield larger errors for S than for IWC.

We now focus on developing Z_e–IWC and Z_e–S relationships, combining the data from all three cases. Ideally, the $m(D)$ relationships that yield approximately the same values of IWC as were measured (e.g., H2013 and BF) would, with appropriate backscatter cross sections, yield approximately the same values of Z_e as were measured, although we noted that this was not the case when examining the data from each case individually. Figure 9 compares the measured reflectivities with those derived assuming the Mie-spheres model for the four $m(D)$ relationships cited. We also use the T-matrix spheroidal backscatter cross-section model discussed in section 3a.

At X band, the difference between Z_e measured and calculated (ΔdBZ_e) is nearly the same for both backscatter models, implying little shape dependence (Figs. 9a,b). The H2013 and BF $m(D)$ relationships produce negative ΔdBZ_e values, consistent with the results expected from Figs. 5a and 5b. Likewise, the TRMM and CF $m(D)$ relationships produce the expected results. The TRMM relationship provides a good match with the X-band reflectivity because the masses from that parameterization are lower than those from the other three relationships.

For W band, the negative ΔdBZ_e values are more extreme than those at X band, a result that was found in Figs. 6a–c, and the magnitude of the error increases with

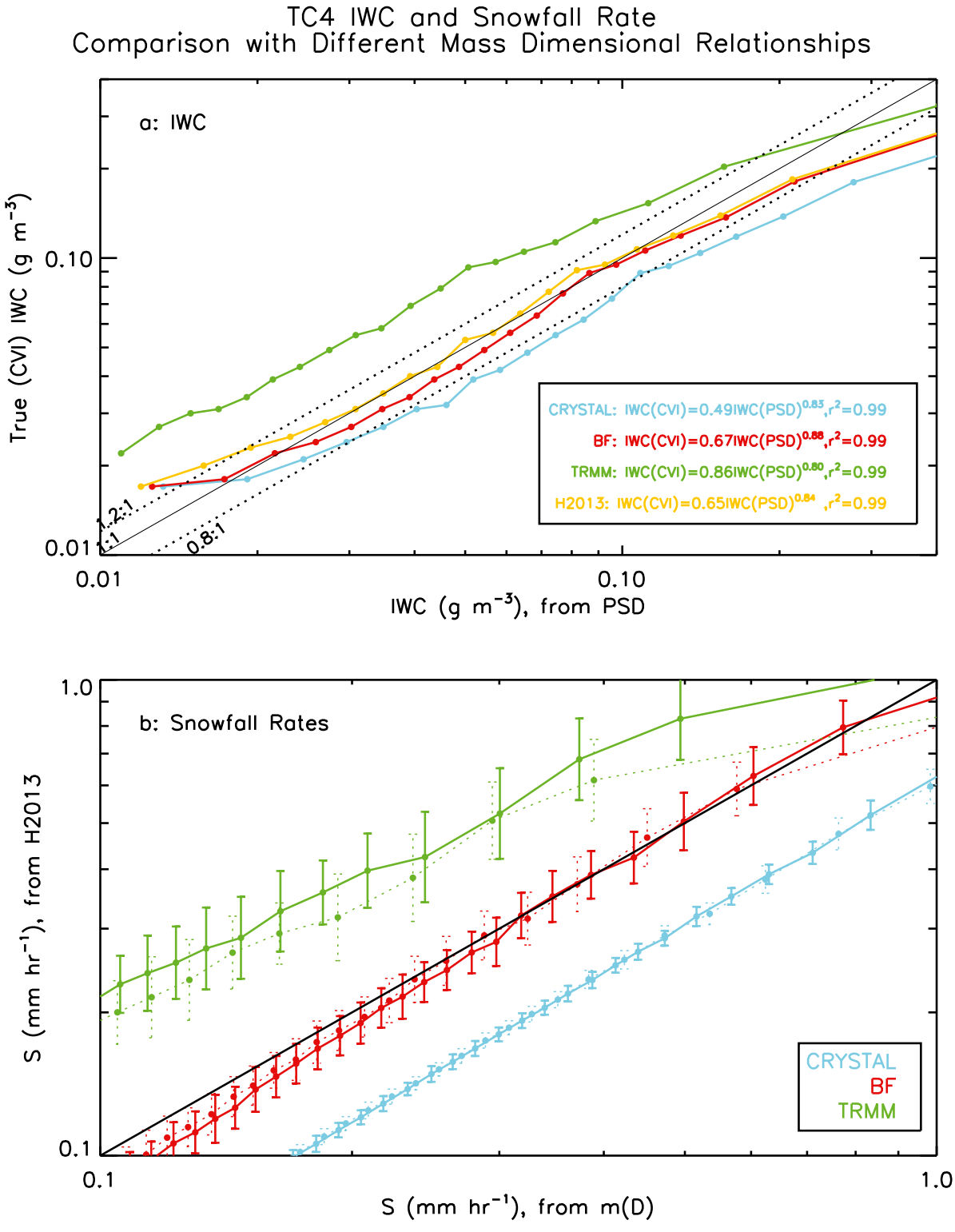

FIG. 7. (a) Comparison of IWC derived from the PSD for the collocation times using different $m(D)$ relationships [CF (light blue), BF (red), TRMM (green), and H2013 (yellow)] with the measured IWC for the three TC4 cases combined. The two dotted black lines and the solid black line show ratios of 0.8, 1.0, and 1.2, representing errors of −20%, 0%, and 20%, respectively. Points along the x axis represent the median value of the IWC in 20 intervals, each interval having the same number of data points; the y axis represents the median value of IWC_{CVI} in that interval. Curve fits, and goodness of fits, are shown for each $m(D)$. (b) Snowfall rates calculated from the different $m(D)$ relationships compared with those derived from the H2013 relationship. The dotted lines show the relationship assuming that the ice particle area ratio is 1.0 rather than the measured values.

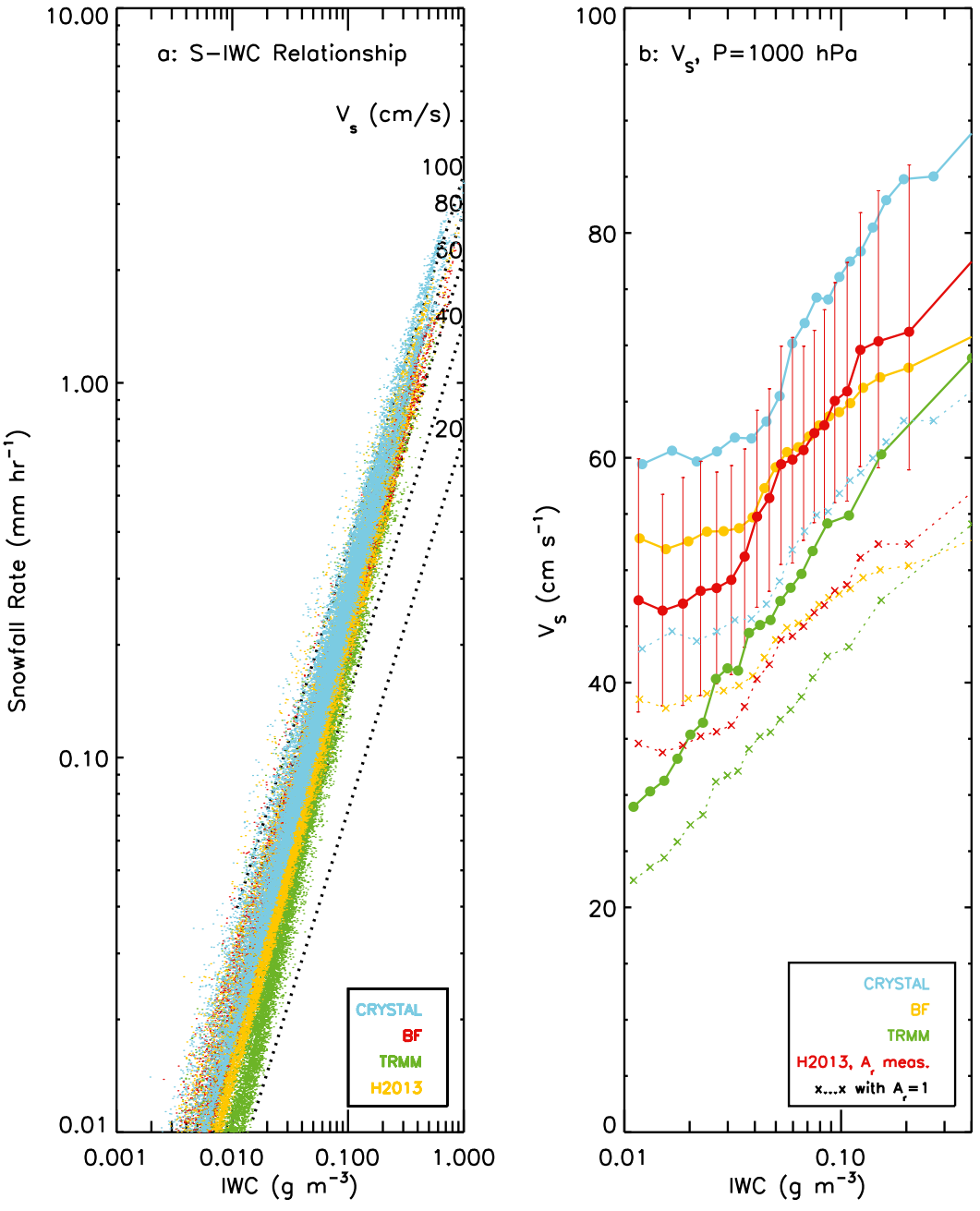

FIG. 8. (a) IWC vs S with lines for different mean snow-rate-weighted terminal velocity (V_s) values ranging from 20 to 100 cm s^{-1}. (b) IWC vs V_s from Eq. (8) as derived from the four $m(D)$ relationships. Also shown are curves assuming that the area ratio is unity.

decreasing Z_e (Figs. 9c,d). The Mie-sphere approximation yields Z_e values that are about 2 dB closer to the measurements. A disturbing trend is noted for $Z_e >$ 0 dBZ, however. Whereas the comparisons at X band have relatively flat ΔdBZ_e values, the ΔdBZ_e at W band are increasingly more positive. This might be in part due to the fact that the T-matrix-based spheroidal model produces reflectivity values that are increasingly biased low as the contribution of larger particles into total backscatter increases.

Given the mismatch between the measured and derived Z_e values, our approach is to develop relationships that are based on the direct measurements, as well as from the PSD, using these different $m(D)$ relationships.

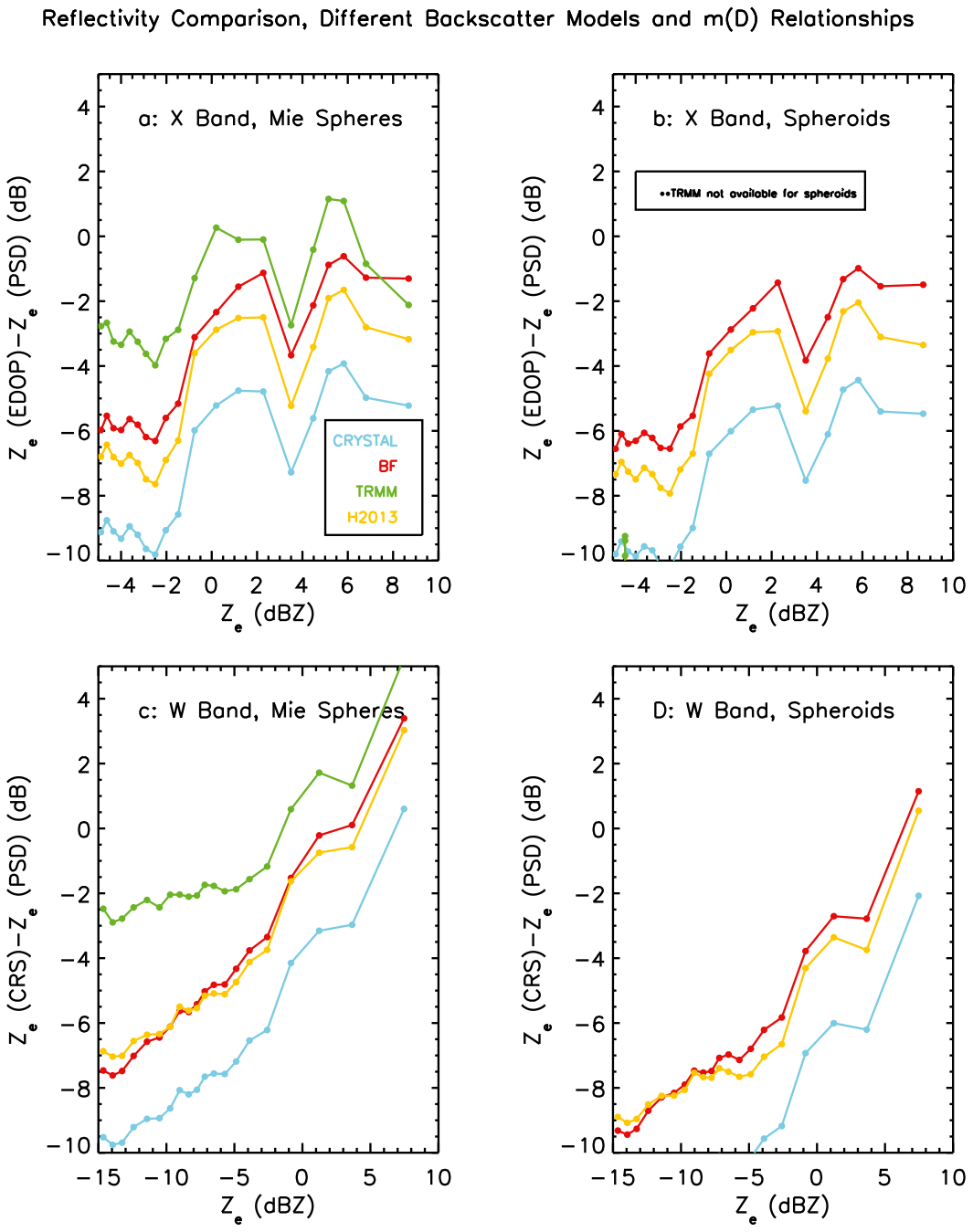

FIG. 9. Calculated (a),(b) Z_e (EDOP) − Z_e (PSD) vs Z_e for X band and (c),(d) Z_e (CRS) − Z_e (PSD) vs Z_e for W band from the four different $m(D)$ relationships (colors). Panels (a) and (c) show the calculations assuming Mie spheres, and (b) and (d) show the values using T-matrix calculations assuming spheroids with a particle aspect ratio of 0.6. The reflectivity given along the x axis is the measured reflectivity.

We now relate the measured and calculated IWCs to the measured X- and W-band reflectivities and to earlier relationships. To simplify the comparison of our results with those developed earlier, we will only show the curve fits to our data and not the individual data points. The X-band Z_e–IWC relationships developed for the CVI and from the PSDs using the H2013 $m(D)$ relationship, along with the fitted curves, are compared in Fig. 10a. The slopes in the relationships are nearly the same (0.422 vs 0.424) and differ by about 12% across the range of reflectivities. If we take the CVI relationship and then calculate the range of IWCs

sampled with the X-band radar, the implied range is 0.098–0.46 g m^{-3}. The relationship developed by Heymsfield et al. (2005), using Z_e (X band) and IWC_{CVI} measured during CRYSTAL-FACE, yields higher values of Z_e for given values of the IWC. This result is likely due to sampling the outflow of a vigorous convective storm, producing larger particles than observed here.

Figure 10b compares the Z_e–IWC fitted curves using the four $m(D)$ relationships with the one derived from the CVI. As found from the earlier comparisons, the BF relationship agrees well with the CVI and H2013 relationships, while CF gives values of IWC that are too large and TRMM gives values that are too small.

The IWCs cover a wider range of observed Z_e for W band than for X band. The relationship developed between Z_e measured at W band and IWC_{CVI} for IWC > 0.01 g m^{-3} has a steeper slope than for X band; this result is due to non-Rayleigh scattering effects at the higher reflectivities (Fig. 11a). The different slopes at the two wavelengths imply that a single Z–IWC relationship for W band across all reflectivities found for W band is not appropriate.

As seen from the curve fit to the CVI data, the range of IWCs covered by the W-band radar are $0.03 <$ IWC $<$ 0.5 g m^{-3}. The slope of the relationship derived from the PSDs is not as steep as for the CVI, and the IWC_{PSD} curve crosses over the IWC_{CVI} curve at -6 dBZ. We believe that this obvious overestimate in the mass of the particles when IWC < 0.089 g m^{-3} is the reason why the calculated reflectivities become increasingly negative than the measured values where $Z_e < -6$ dBZ.

The Z_e–IWC relationships developed from the *CloudSat* global database using the retrieval algorithms 2C-SNOW and 2C-ICE are plotted in Fig. 11a for two temperature intervals, $-50°$ to $-40°$C and $-10°$ to 0°C. Given that the temperatures measured by the DC-8 aircraft during the overpasses were generally in the $-20°$ to $-50°$C range, the *CloudSat* observations for temperatures of $-50°$ to $-40°$C would be more appropriate for comparison with our dataset. In the range $-10 < Z_e <$ 0 dBZ, there is about a factor of 3 difference in the IWCs from the in situ measurements and the 2C-SNOW but good agreement with the 2C-ICE and Matrosov and Heymsfield (2008) technique data, especially at higher reflectivities.

Numerous Z_e–IWC relationships for W band appear in the literature, derived from either 1) PSDs observed or presented in the literature, in most cases using $m(D)$ relationships that are available in the literature, or 2) using output from numerical models. They are largely developed for stratiform ice clouds. In Fig. 11a, some of these Z_e–IWC relationships are replotted in IWC–Z_e coordinates. Although there is a wide spread in the relationships, all yield lower IWCs for a given Z_e than we observe in this study. This is not due to our sampling in outflow ice cloud rather than for stratiform cloud, because these situations would likely lead to higher IWCs for a given Z_e because of more small particles. Instead, we suggest that this result is due to two factors: 1) some of the relationships integrate the assumed PSD with diameter limits from 0 to infinity, which would produce more reflectivity than would be found with a limit to the maximum diameter, and 2) ice particle densities that are higher than are implied by the CVI data, producing the same effect. Although the radar backscatter cross sections used for the relationships may not accurately represent the particles in clouds, this is not likely the problem because the disagreements are largest at the low reflectivities where there would be little non-Rayleigh scattering.

The Z_e–IWC size relationship derived from the CVI data is compared in Fig. 11b with the relationships derived from the various $m(D)$ relationships. It is interesting to note that the curve for the CVI has a somewhat steeper slope than the H2013 and BF curves, for unexplained reasons. The curve for TRMM is parallel to the CVI curve, suggesting that an increase in the coefficient k in Eq. (6) would produce good results.

The relationship between the snowfall rate and measured X-band reflectivity is derived from the PSDs, as described earlier (Fig. 12). Rather than using the atmospheric pressure that was measured during the in situ sampling, a pressure of 1000 hPa is assumed in order to conform to most other Z_e–S relationships. The snowfall rates implied by the fitted curve are in the range of 0.2–0.88 mm h^{-1}; the upper limit is quite low.

An important consideration that should not be overlooked is that ice particles in the airstream flowing through the arms of the imaging probes (when the probe is looking downward on the particles) torque upward, potentially leading to an underestimation of their maximum particle size (King 1986) and a decrease or increase in their area/area ratio. We have evaluated the potential effect on the terminal velocity (but not on the reflectivity, as that would be complex because of nonlinear scattering effects). We have examined the size dependence of the mean area ratio for the ice regions of the TC4 clouds by increasing/decreasing the averages by $\pm$20% (fairly extreme). We have also decreased the particle diameter by 10%. On average, doing so leads to 11% decrease/4% increase in V_t. As a sensitivity study of the effects of an extreme case in the estimates of the snowfall rates that follow, we assume that $A_r = 1.0$ and there is no change in particle diameter.

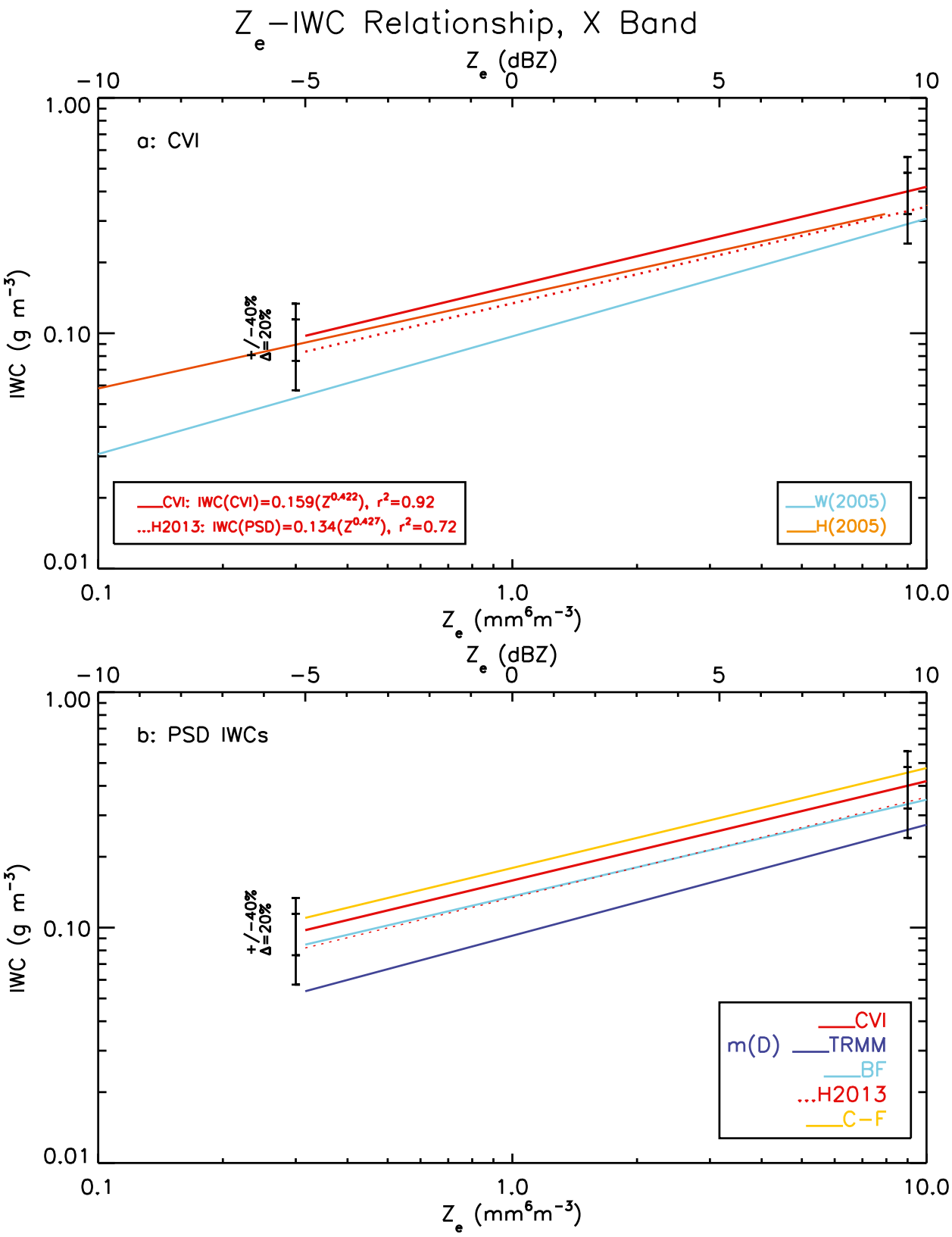

FIG. 10. Comparison of the measured values of X-band reflectivity (from EDOP) with (a) IWC_{CVI} and (b) IWC_{PSD}. Also shown are least squares fits to these data. The earlier parameterizations at X band are Wang et al. (2005) [W(2005)] and Heymsfield et al. (2005) [H(2005)], which is a fit to the CRYSTAL-FACE data. Deviations of ±20% and ±40% from the CVI values are shown at the indicated IWC in each panel.

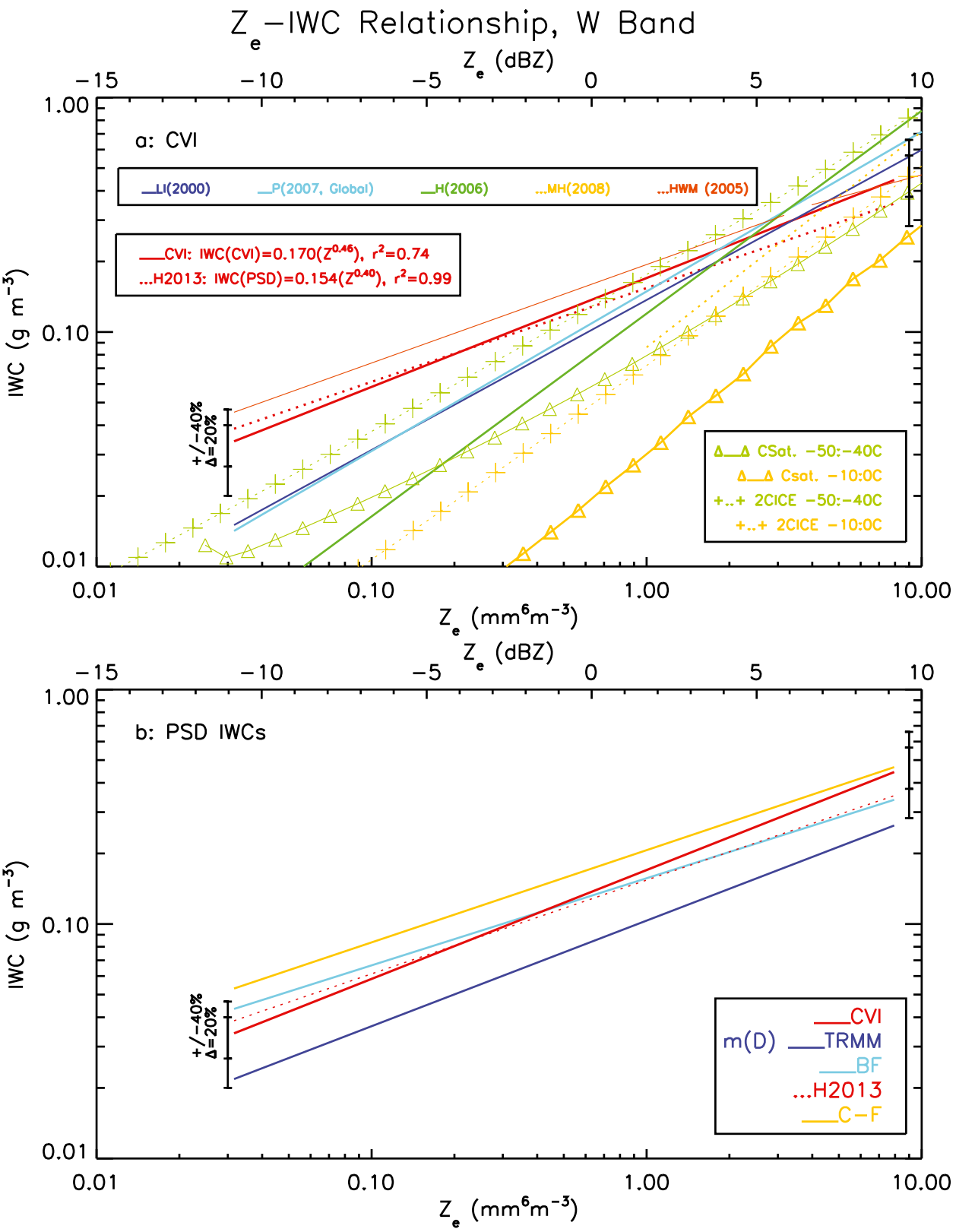

FIG. 11. As in Fig. 10, but for W band. In (a), averages for the *CloudSat* retrieval algorithms 2C-SNOW (CSat.) and 2C-ICE are also shown for two temperature ranges. The parameterizations at W band are Liu and Illingworth (2000) [LI(2000)], Protat et al. (2007) [P(2007)], Hogan et al. (2006) [H(2006)], Matrosov and Heymsfield (2008) [MH(2008)], and Heymsfield et al. (2005) [HWM (2005)].

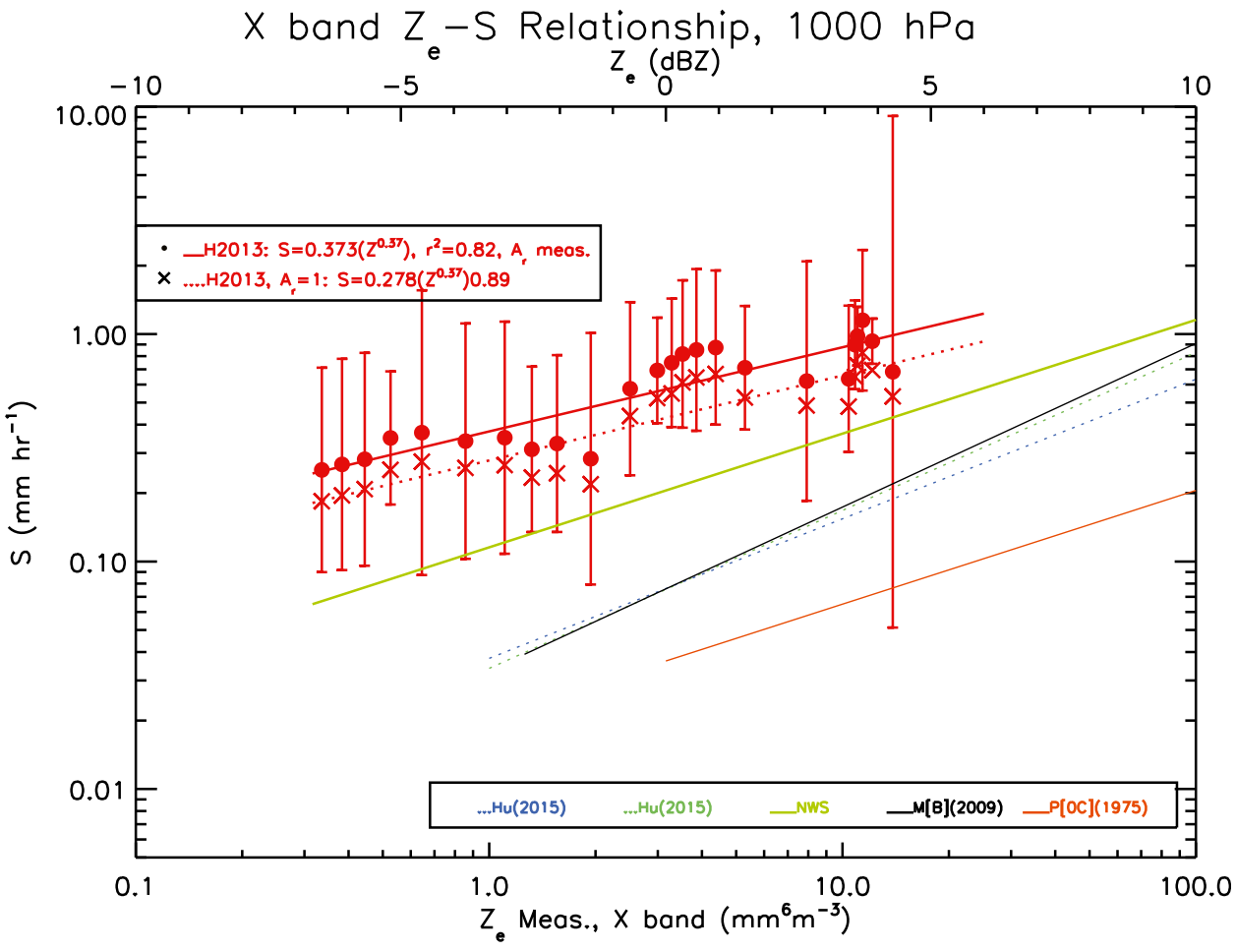

FIG. 12. Snowfall rates, calculated for particles falling at a pressure level of 1000 hPa, as a function of EDOP (X band) radar reflectivity (shown as curve fits) from the TC4 observations derived from the H2013 $m(D)$ relationship using the measured A_r (solid lines) and A_r = 1.0 (dotted lines). The data points, and times signs and error bars, are median values of S in intervals of Z_e using this $m(D)$ relationship. Vertical bars show intervals of ±20% and ±40% deviations from that curve at two values of Z_e, along with the curve fit. The earlier relationships shown are Huang et al. (2015) [Hu(2015)] for C-band radar for two case-study days, identified with different colors; National Weather Service S-band snow relationship (NWS); Matrosov et al. (2009) using the PSD from Braham (1990) [M(B)(2009)]; and Puhakka (1975) [P(0C)(1975)].

Earlier Z_e–S relationships are shown in Fig. 12. One was developed for X band by Puhakka (1975) on the basis of measured Z_e and measured snowfall rate (with appreciable time averaging); two were developed for C band by Huang et al. (2015) using a 2D video disdrometer in comparison with rain gauge and radar measurements; Matrosov et al. (2009) used $m(D)$ and PSD relationships, which they evaluated against radar, precipitation gauge, and Hotplate data; also plotted is a relationship used by the National Weather Service (Vasiloff et al. 2013) for S-band measurements, and one derived by Puhakka (1975). In general, these relationships were developed or evaluated where $Z_e > 15$ dBZ, whereas in our study $Z_e < 10$ dBZ. Even though a comparison over the same range of reflectivities is not possible, the plots suggest that for a given value of Z_e our estimated S are considerably larger than those derived from earlier studies, even if we assume that all particles have an area ratio of 1.0.

The Z_e–S relationship developed for W band from the H2013 $m(D)$ relationship yields higher values of S for a given reflectivity than those found from earlier studies, except for the one identified as SS in Fig. 13. Assuming an A_r of unity has little effect on the resulting relationship. Because of the range of reflectivities considered, non-Rayleigh effects are probably small, and this is suggested by the similarity between the Z_e–S fitted relationships for X and W bands. (Fig. 13a vs Fig. 12a). The range of S implied by the fitted curve is 0.08–1.19 mm h^{-1}; the upper limit is quite low. Earlier relationships yield lower values

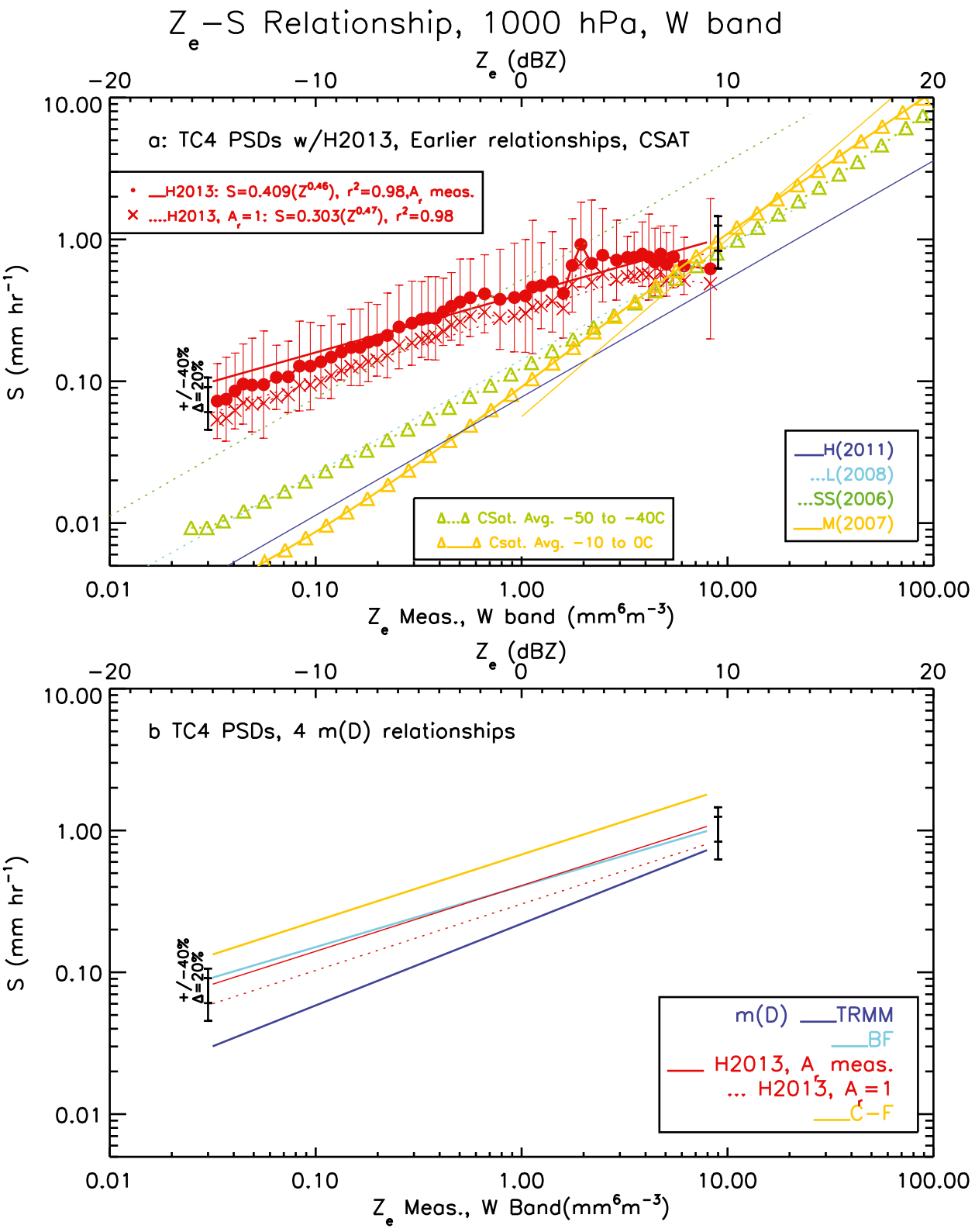

FIG. 13. As in Fig. 12, but for W band. In (a), averages based on the *CloudSat* 2C-SNOW are shown for two temperature intervals. The relationships shown are from Hiley et al. (2011) [H(2011)], Liu (2008) [L(2008)], Surassavadee and Staelin (2006) [SS(2006)], and Matrosov (2007) M(2007).

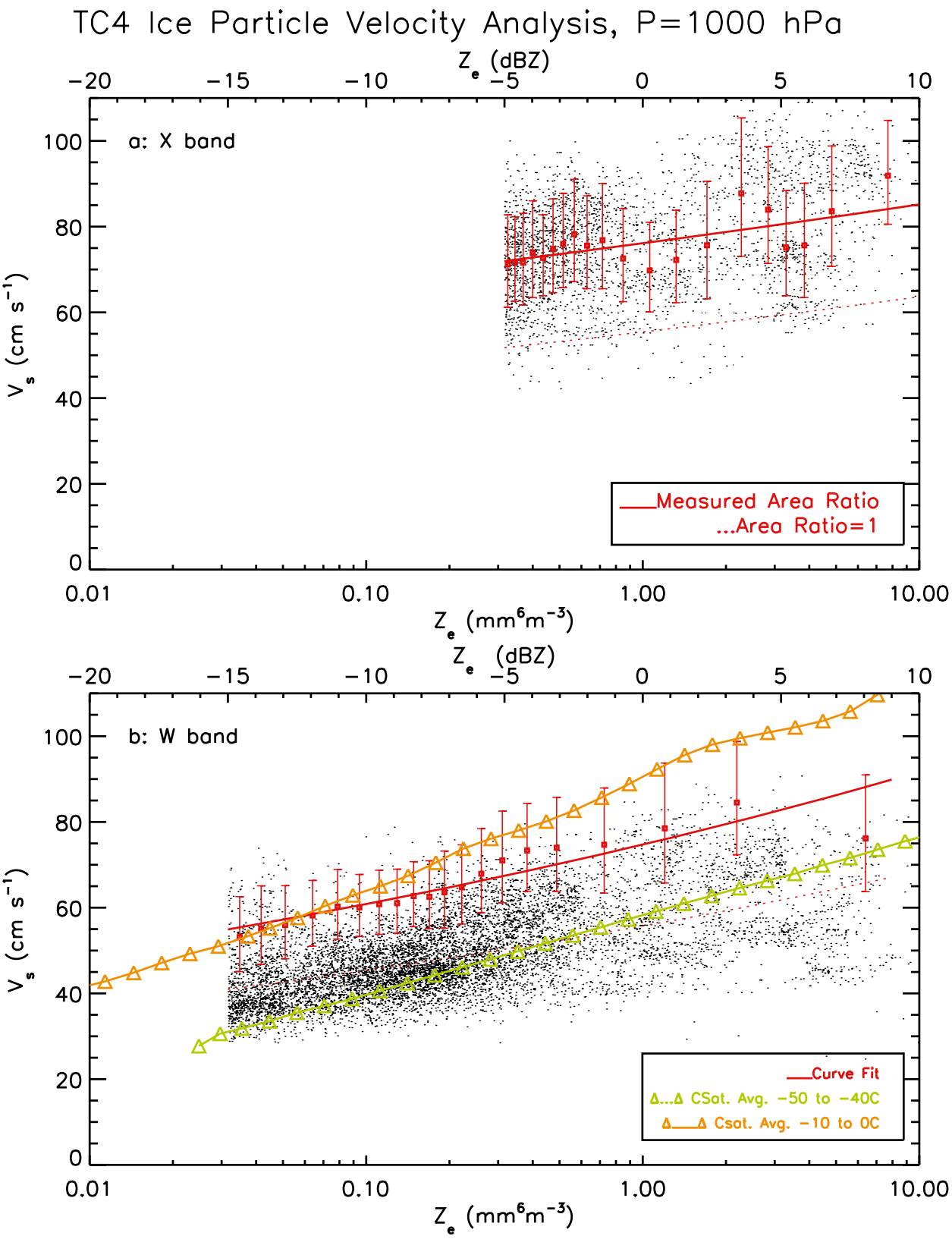

FIG. 14. Terminal velocities V_s derived from a combination of snowfall rate and IWC as a function of Z_e measured at (a) X band and (b) W band, for the TC4 data. The V_s curves for the H2013 assume two area ratios, those measured (solid red) and those assuming a value of 1.0 (dotted red). The black points indicate the measured area ratios. In (b), the values derived from 2C-SNOW are shown.

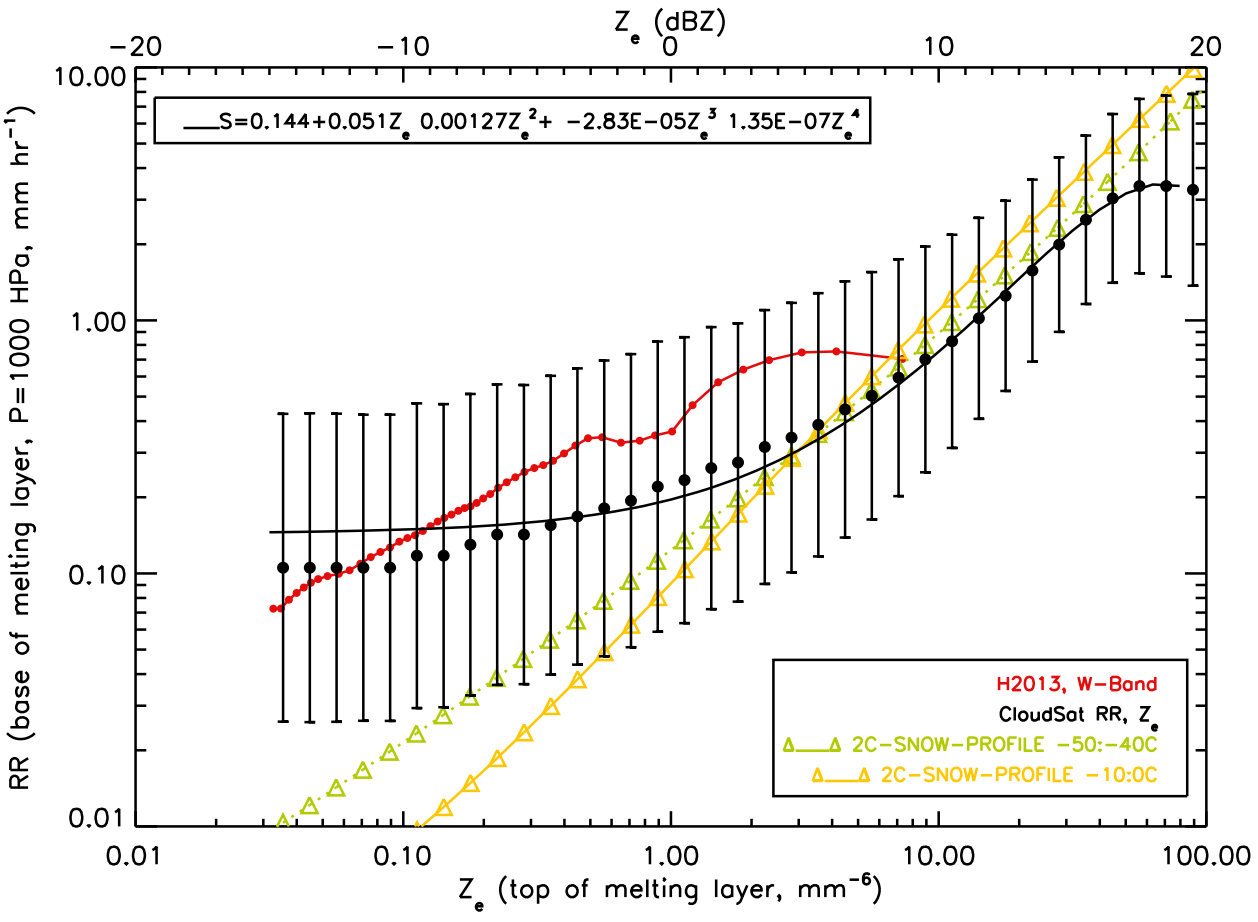

FIG. 15. Rain rate retrieved for a height just below the melting layer as a function of the reflectivity at the top of the melting layer, from *CloudSat* data. A fourth-order polynomial is fitted to the data. Shown for comparison are the *CloudSat* 2C-SNOW averages for the two temperature ranges.

of S than those derived from the TC4 data (Fig. 13a). Also, the temperature-dependent average S from the *CloudSat* 2C-SNOW are one-half or less than those derived from the TC4 data for the same reflectivity. This point will be discussed in more detail in section 4. There are no surprises in how the Z_e–S curves compare for the four $m(D)$ relationships (Fig. 13b).

Although the terminal velocity is not likely to be the primary factor responsible for the differences in our Z_e–S relationship and those from earlier studies, we can check on the realism of our estimates of V_t. An estimate of the mass-weighted fall speed normalized to a pressure level of 1000 hPa V_s is from Eq. (8). Figure 14a shows that V_s as a function of Z_e at X band for the TC4 dataset is indeed quite large, ~90 cm s^{-1}. Increasing the A_r to unity does make a sizeable difference, but this is an unrealistically high value. In Fig. 14b, V_s as a function of Z_e at W band for the TC4 data is compared with those from the *CloudSat* 2C-SNOW analysis. For the temperature range −50° to −40°C, the TC4 V_s values are about a factor of 2 larger than the *CloudSat* retrieved values.

Also shown in the figure is V_s as a function of Z_e derived based on the mean A_r as a function of size for the TC4 particles, with a curve fit to those data. These fit quite well to $A_r = 0.4$ using the $m(D)$ relationship of H2013, close to the averages for the TC4 data. The V_s are higher than are deduced, for example, using 2D video disdrometers at the ground (Huang et al. 2015). The A_r of the particles they examined, looking from the side rather than from the top, are about 0.7; for particle sizes of 1 mm and below, the particle masses are about 1.7 times as large as those we use for the V_s calculations. The V_s derived from the assuming an A_r of 0.7 fits closely to the Huang et al. (2015) data. Although the particles they sampled have higher masses, the A_r in the direction of the fall of the particles may be larger than they measured from the side. In any event,

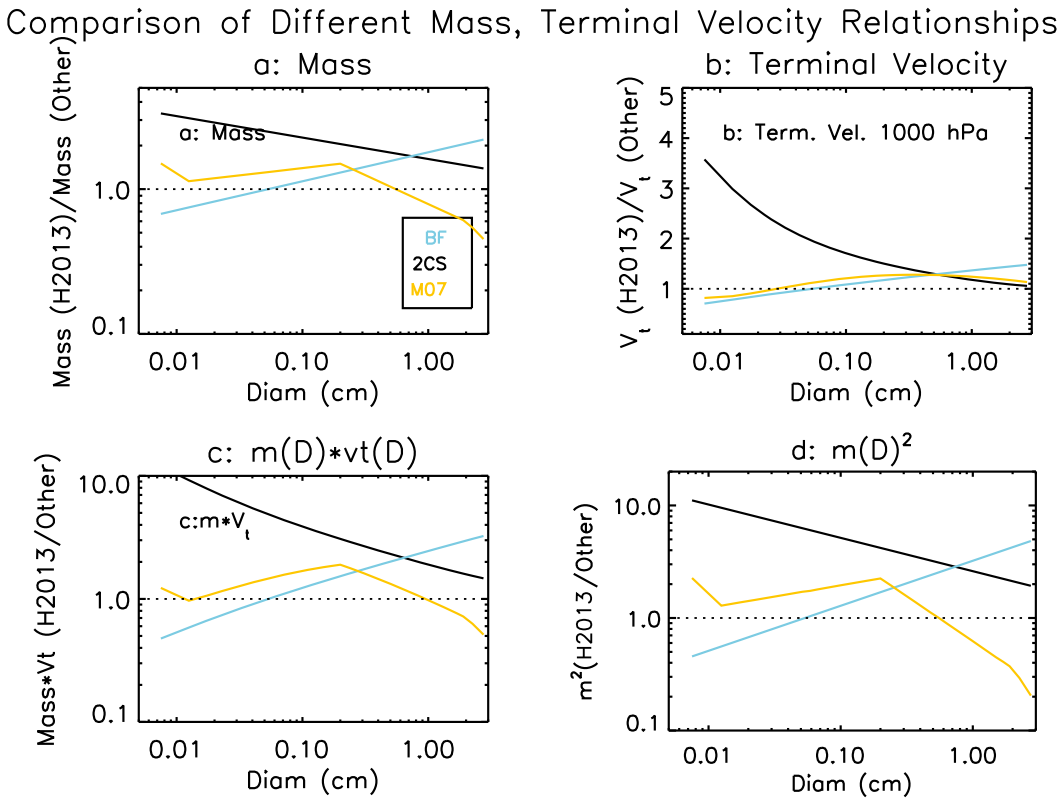

FIG. 16. Comparison of the (a) particle mass, (b) terminal velocity, (c) product of mass and terminal velocity, and (d) mass squared as illustrated by the H2013 algorithm divided by those given by the BF, 2C-SNOW, and M07 approaches.

we conclude that potential errors in our estimates of the particle terminal velocities do not fully explain the discrepancy between our S and those from the *CloudSat* analysis.

4. General snowfall rate–reflectivity relationships at W band (*CloudSat*)

CloudSat-derived rainfall rates (R) at a height just below the bottom of the melting layer are related to the radar reflectivity measured at a height directly above the melting layer where the freezing level height is from the *CloudSat* 2C-PRECIP-COLUMN product and is identified using collocated reanalysis temperature profiles (Haynes et al. 2009). These are for clouds identified as "stratiform." To the authors' knowledge, this approach has not been used before. Assuming that the precipitation rate across the melting layer is approximately constant, then Z_e and R, and thus Z_e and S, can be related directly. Heymsfield et al. (2015) calculated the snowfall rate at the top of the melting layer and compared this with the rainfall rate at the bottom of the layer in cases in which the relative humidity through the layer ranged from near water saturation to considerably below water saturation. The S and R agree to better than 50%, which we consider to be quite good given the uncertainties in the rates due to factors such as the $m(D)$ relationship used to estimate the masses of the snow particles. Also, uncertainties in the retrieved rainfall products from *CloudSat* will contribute errors to the estimated values of R. Given these potential sources of error, we believe that this analysis can provide a check on the Z_e–S relationship derived from the TC4 data and extend it to much lower and higher reflectivities. Also, we can compare these results with the 2C-SNOW snowfall rates.

For the *CloudSat* dataset, there are more than 11 million data points. These are summarized in Fig. 15, in the form of mean values and standard deviations obtained for reflectivities from −20 to 20 dBZ. Rain water contents were taken from the *CloudSat* 2C-RAIN-PROFILE product (Lebsock and L'Ecuyer 2011; Mitrescu et al. 2010) for a height 1 km below the estimated freezing level. Rain water contents were converted to rain rates assuming a Marshall–Palmer distribution (Marshall and Palmer 1948). Also shown are the values found from the T4 data using the H2013 $m(D)$ relationship. These agree well with those from

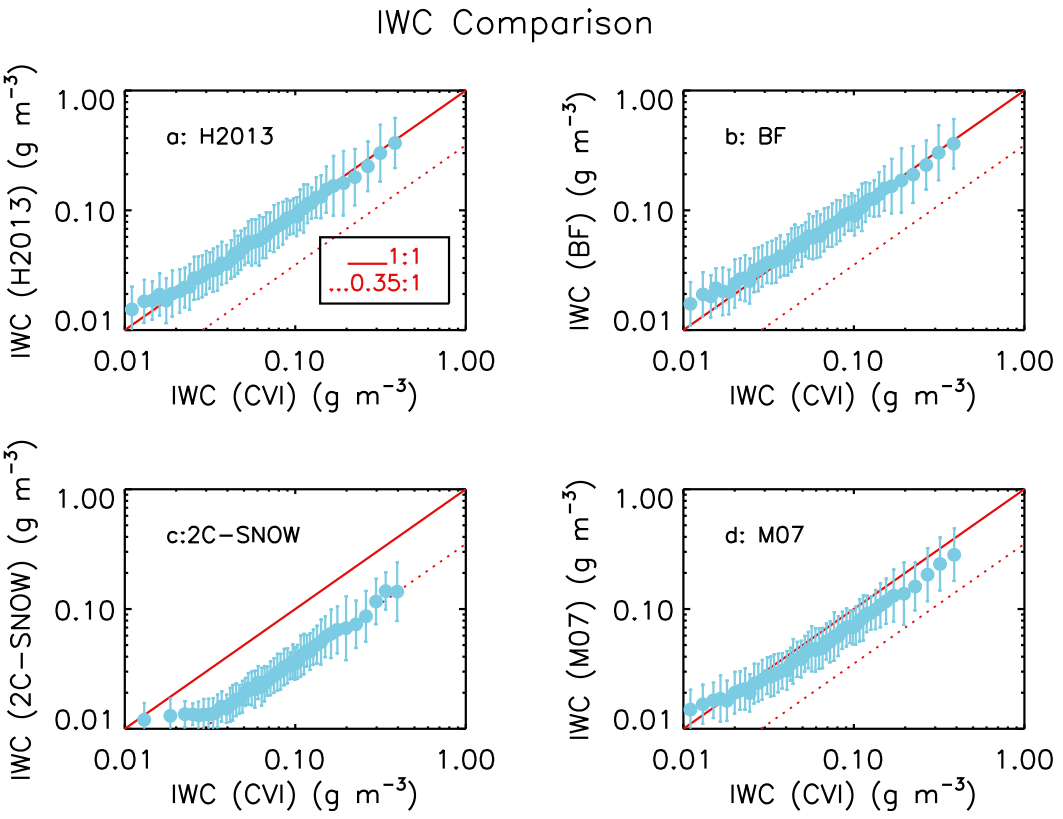

FIG. 17. Comparison of the IWC derived from the CVI with the (a) H2013, (b) BF, (c) 2C-SNOW, and (d) M07 m (D) relationships for the times of the aircraft collocations on three days during TC4.

the Z_e–R relationship, at least for Z_e from −10 to 10 dBZ. Although the 2C-SNOW snowfall rates agree well with those derived from the Z_e–R relationship, the snowfall rates are increasingly underestimated by 2C-SNOW where $Z_e < 8$ dBZ.

5. Discussion

Our Z_e–IWC relationship was derived directly from measurements; our Z_e–S relationship was derived from a mass–dimensional relationship that yielded IWCs consistent with the direct measurements but that overestimated X- and W-band reflectivities for a majority of the collocations. There were no obvious inconsistencies found when evaluating the terminal velocities. The Z_e–IWC relationship derived from the *CloudSat* 2C-ICE algorithm, and obtained for four years of data, agrees quite well with our TC4 Z_e–IWC relationship. The Z_e–IWC and S–Z_e relationships derived from 2C-SNOW yield lower IWCs and S values for a given Z_e over the range sampled here; similarly, this was found by comparison with many of the earlier studies.

The discrepancies noted could be due to differences in measured or assumed ice particle mass. We can examine how the $m(D)$ relationship affects the calculated S and the Z_e–S relationship by drawing upon the assumptions used in the 2C-SNOW algorithm. The 2C-SNOW models particle masses and horizontally projected areas as power laws whose parameters are determined from analyses of ground-based observations of lake-effect and synoptically driven snow (Wood et al. 2015). In that algorithm, $m = 0.0033D^{2.25}$, and the V_t are calculated (assuming a pressure of 1000 hPa for the analyses presented here) from the masses and horizontally projected areas using the formulation of Mitchell and Heymsfield (2005). A fit to those velocities, although a fit is not used in the algorithm, yields $V_t = 149D^{0.52}$ (cgs units).

Figure 16a compares the size dependence of the mass given by the H2013 relationship divided by the mass given by the 2C-SNOW algorithm and BF and M07 relationships, respectively. Also compared are the ice particle masses used in the Z_e–S relationship developed by M07. The 2C-SNOW masses are considerably below those of H2013, BF, and M07, particularly in the range 100–1000 μm, where most of the IWC is contained in these samples (Figs. 3d–f). Because mass enters into the estimation of the V_t, it is not surprising that the ratio of the V_t derived from the H2013, BF, and M07 approaches

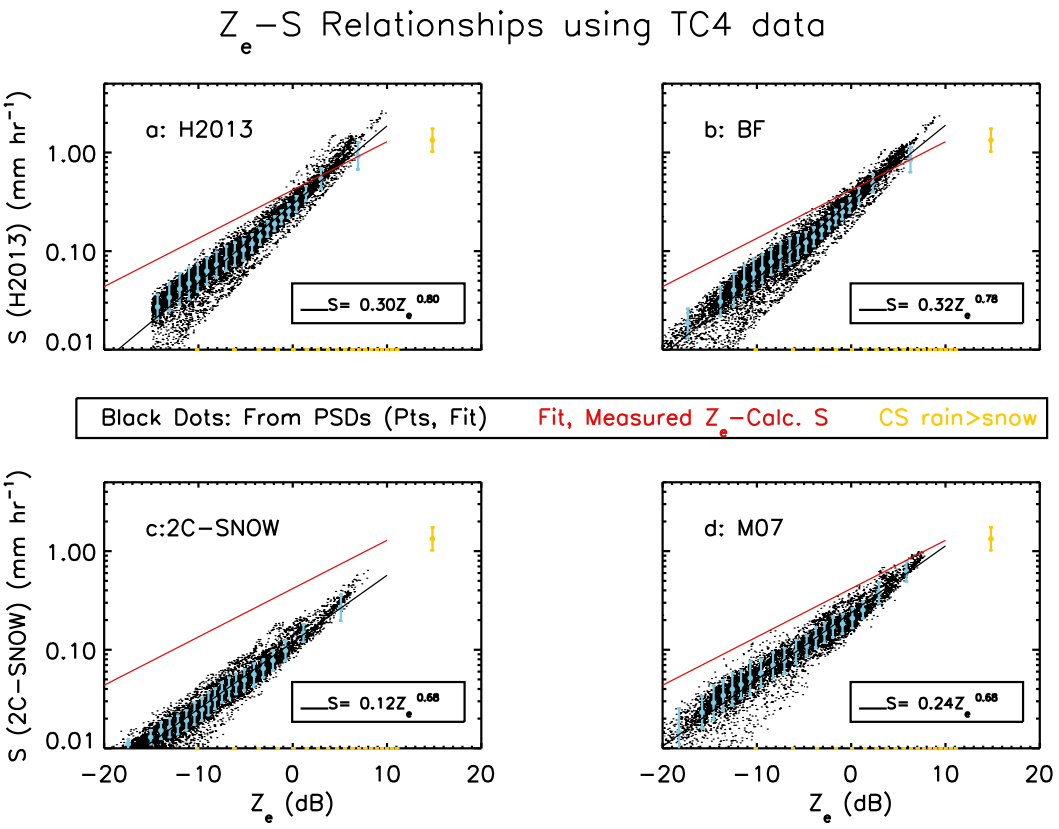

FIG. 18. Comparison of snow-rate–reflectivity relationships derived from the PSDs for W band using the $m(D)$ and V_t relationships of (a) H2013, (b) BF, (c) 2C-SNOW, and (d) M07. Backscatter cross sections for H2013, BF, and M07 are derived using their $m(D)$ relationship assuming that particles are oblate spheroids of aspect ratio 0.6; those for 2C-SNOW are derived using that algorithm. Curve fits to the data are also given. Also shown are the Z_e–S relationships derived from the TC4 data and the method that compares rainfall rate at the bottom of the melting layer with the reflectivity at the top of the layer.

is much larger than those from the 2C-SNOW V_t (Fig. 16b). An A_r of 0.4 is used to calculate V_t for the H2013 and BF masses. As expected from Figs. 16a and 16b, S is quite low for the 2C-SNOW algorithm relative to those derived for the other three methods (Fig. 16c). The radar reflectivity is approximately proportional to m^2, assuming that the particles act as Rayleigh scatters (for smaller particle sizes). Not surprisingly, this term is low relative to those derived using the other two $m(D)$ relationships (Fig. 16d). A comparison of Figs. 16c and 16d suggests that the $m(D)^2$ discrepancy is relatively close to the $m(D)V_t(D)$ discrepancy. Clearly, errors in $m(D)$ will produce errors in $m(D)^2$ and $m(D)V_t(D)$ that are correlated; however, these errors will likely not cancel out, because when a PSD is considered, the weighting of the size distribution by mV_t when calculating S is generally different than weighting when calculating Z_e. In addition, backscatter cross sections for nonspherical particles also influence Z_e, in a nonstraightforward way.

Figure 17 shows how the $m(D)$ relationship factors into the calculation of the IWC when the PSD is considered and how this influences the discrepancy. In the figure, the IWC derived from the H2013, BF, 2C-SNOW and M07 $m(D)$ relationships are compared with that measured by the CVI. The H2013 and BF $m(D)$ relationships both provide a good match with the $\mathrm{IWC_{CVI}}$, with little difference noted between the two (Figs. 17a,b). The IWCs derived from the M07 $m(D)$ relationship are about 20% lower than measured (Fig. 17c). By contrast, there is a factor of about 3 discrepancy between the IWC measured and from the 2C-SNOW approach, similar to that found with the comparison of the $m(D)$ relationships in Fig. 16a, for particle sizes of 100–1000 μm.

Figure 18 uses the PSDs, $m(D)$ relationships, and backscatter cross sections to develop Z_e–S relationships for the four different methods. For the H2013 and BF approaches, the backscatter cross sections are derived as discussed earlier for the TC4 data. The cross sections in

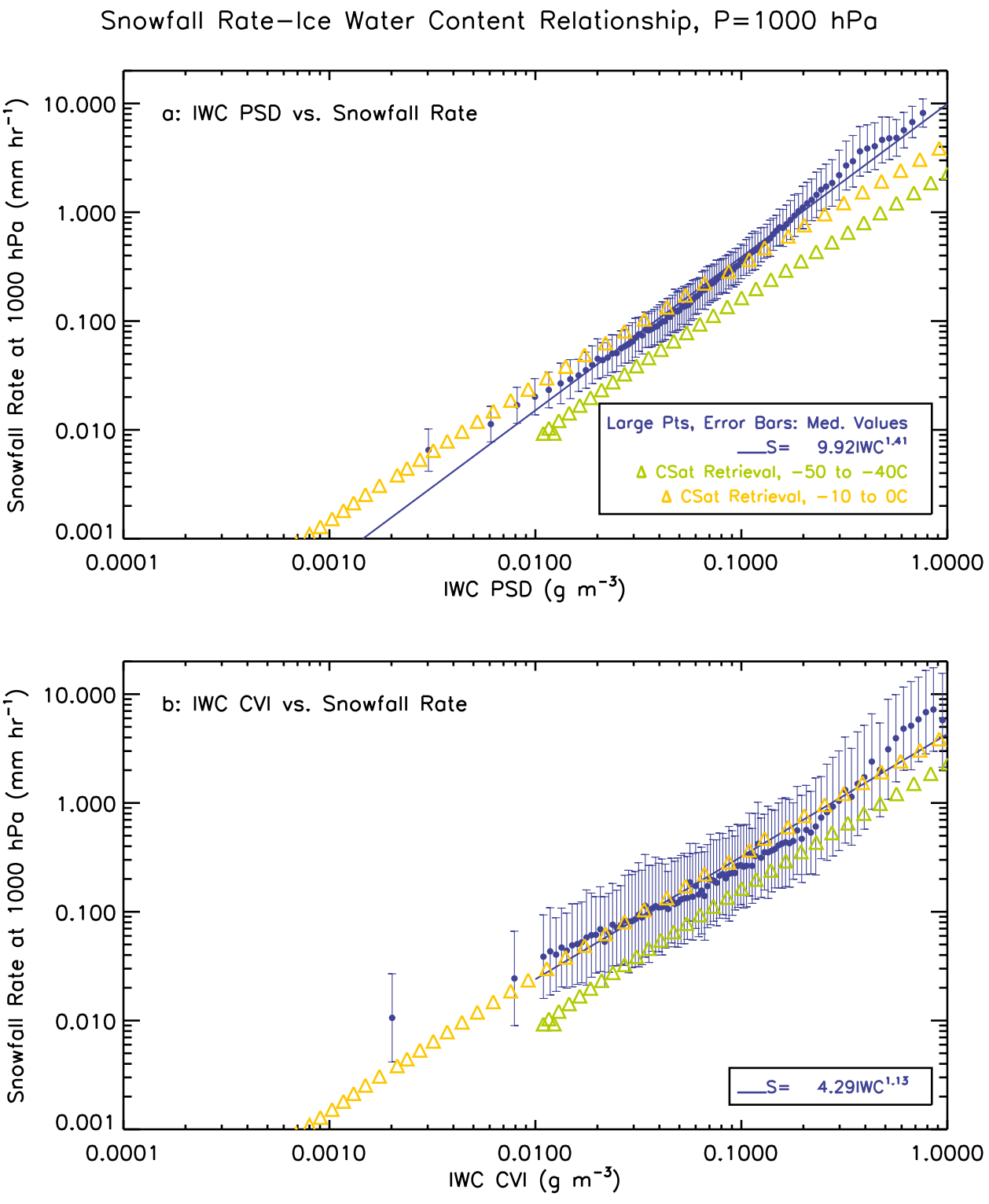

FIG. 19. Snowfall rate as a function of the IWC derived from a large dataset (1×10^6 km in situ sampling; Heymsfield et al. 2013), where the terminal velocities are calculated assuming a pressure level of 1000 hPa. Median values with error bars are shown in blue, along with a curve fit to the values. Values derived from the *CloudSat* 2C-SNOW analysis, derived for a pressure level of 1000 hPa and for the two different temperature ranges are also shown. (a) IWC calculated from the particle size distributions, and (b) IWC measured by the CVI.

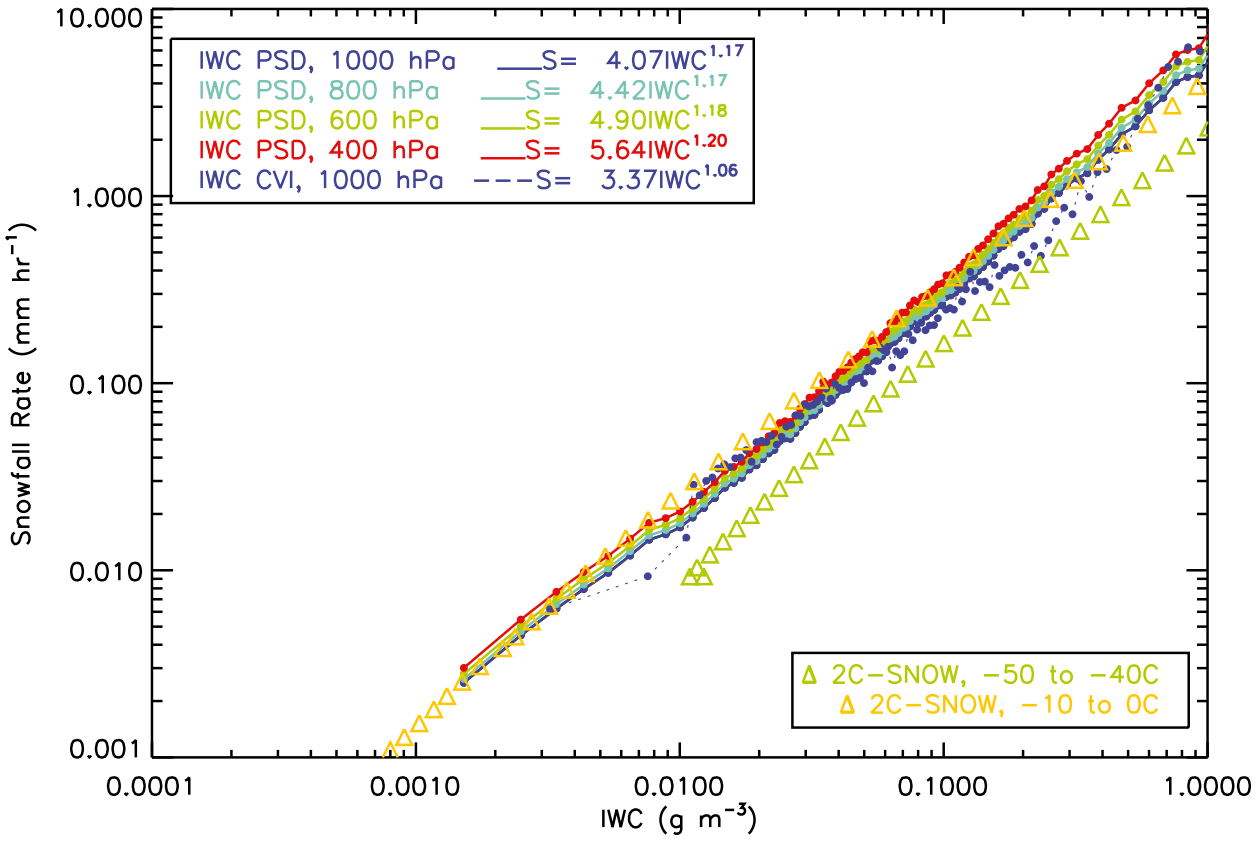

FIG. 20. Relationship between snowfall rate and IWC, where for the PSD approach different pressure levels are used to calculate S.

M07 are based on that $m(D)$ relationship, and those for the 2C-SNOW approach use those developed in Wood et al. (2015). Also shown are the values derived by relating the rain rate at the base to the reflectivity at the top of the melting layer, and the quasi-direct Z_e–S relationship developed from the snow rate calculated from the PSDs (H2013) and the collocated CRS radar reflectivities. The calculations using the M07 approach fit the data best, but even so there is still an increasing difference between the calculated and measured Z_e as the reflectivity decreases below about 5 dBZ, mirroring the general findings shown in Figs. 9c and 9d.

Section 3 has shown Z_e–IWC and Z_e–S relationships from a number of studies. These relationships are developed independently and may have used different assumptions to derive particle masses and size distributions. Because the retrieval of IWC has fewer assumptions than the snowfall rate, and thus it is expected to be more accurate (e.g., cf. Figs. 16a and 16c), it is desirable to have a way of directly relating S and IWC. It can be shown analytically that these can be related because the size distributions and the particle masses are the same and because the terminal velocity is a function of the particle size and shape.

In Fig. 19, the S derived for a pressure level of 1000 hPa is related to $\mathrm{IWC_{CVI}}$ for field programs ranging from tropical to Arctic areas. There are a total of more than 600 000 km of in situ sampling (H2013). The snowfall rates are calculated based on particle areas, as was done here. The TC4 dataset is included in this evaluation. Figure 19 shows the relationship between S and IWC is approximately a power law, with log(S) increasing almost linearly with log(IWC). The *CloudSat* 2C-SNOW data for the temperature interval of −10° to 0°C fall almost on top of the points from the large dataset, implying that, if the IWC is known, such as from 2C-ICE, the S can be derived (for a pressure level of 1000 hPa). These can be readily adjusted using the adjustment for pressure from Heymsfield and Westbrook (2010). In Fig. 19b, the snowfall rates are related to the measured IWC. Because these IWCs are independent of the calculated snowfall rates, the relationship between S and IWC is somewhat different. It is preferable to use the data where S and IWC are both calculated from the same $m(D)$ relationship because the resulting errors are reduced even though the $m(D)$ relationship might not be exactly correct.

The S–IWC relationships derived from the PSDs for different pressure levels—1000, 800, 600, and 400 hPa—are

compared in Fig. 20. For a given IWC, S decreases slightly with pressure. The S–IWC_{CVI} relationship yields slightly lower values for S for IWC $> 0.1\,g\,m^{-3}$. The relationship derived from the *CloudSat* 2C-SNOW retrieval for a pressure level of 1000 hPa and temperatures of −10° to 0°C agree quite well with the IWC_{PSD} and the IWC_{CVI} for the same pressure level. This would suggest that the S–IWC relationship is relatively independent of the retrieval algorithm and that the 2C-ICE retrieval of IWC can be used to yield snowfall rates.

6. Summary and conclusions

This study has used nadir-viewing radar measurements from the NASA ER-2 aircraft together with in situ microphysical measurements from the NASA DC-8 aircraft during the TC4 field program to develop Z_e–IWC and Z_e–S relationships. The specific goal of the study was not to develop relationships that are universally applicable to clouds and precipitation remote sensing from satellite-borne radars. Rather, the goal of this study was to test the ability to obtain IWC and S as a function of radar reflectivity at X and W bands from particle size distributions, where the particle mass could be derived accurately using direct measurements of the IWC and particle size distributions–shapes, and the reflectivities at these wavelengths could be measured directly with collocated remote sensing and in situ observations. A key finding of the study is that, even though ice particle masses were constrained by the ice water content measurements, backscatter cross sections derived using two backscatter models were overpredicted. There are several limitations to our study: first, the upper limit of the reflectivities measured was only 10 dBZ, and our study uses a set of data that are for one geographical area during the summer months. Also, our relationships are developed from data in outflow regions, and snow falling to the ground could have different characteristics than that observed aloft.

Specific findings include the following:

- Even with knowledge of the particle mass, reflectivities calculated using Mie-sphere and T-matrix approximations were 2–8 dB too high relative to the collocated radar observations, suggesting that either the masses of the particles >1 mm are too high and that a single power-law-type mass–dimensional relationship does not apply to all particle sizes, and/or the models we used to represent the backscatter cross sections of the particles are inappropriate. Our analysis does suggest that the mass–dimensional relationships are different for the smaller and larger parts of the ice particle populations.
- When applied to the observed PSDs, the H2013 and Brown and Francis (1995) $m(D)$ relationships yielded IWCs that were accurate to better than 20% over the range 0.01 to about $0.5\,g\,m^{-3}$.
- When applying $m(D)$ to observed PSDs to yield IWC and S, errors in $m(D)$ produce larger errors in S than in IWC.
- The *CloudSat* 2C-ICE algorithm yielded a Z_e–IWC relationship that fit the relationship developed from the TC4 data quite well, for similar temperatures.
- The *CloudSat* 2C-SNOW algorithm might underpredict the IWCs and S, for the specific reasons identified. Our study can lead to improvements in the algorithms this retrieval uses.
- A method for deriving Z_e–S relationships, using the idea that there is approximately conservation of mass flux across the melting layer, is developed using almost five years of *CloudSat* data.
- Pressure-dependent relationships for directly relating retrieved IWC—a parameter that has fewer variables than S and is thereby less prone to error—to the S is developed from a vast library of globally derived direct measurements of IWC.

In a future study, we will develop Z_e–IWC and Z_e–S relationships using Ku- and Ka-band radar data that are collocated with in situ aircraft measurements from several field programs and cover a wider range of reflectivities. As part of that effort, we will attempt to quantify and explain differences in the relationships developed from the in situ data and those derived in earlier studies and from retrievals developed for the GPM Ku- and Ka-band measurements; we will also attempt to quantify potential errors in backscatter cross-section models.

Acknowledgments. The authors thank Aaron Bansemer for his invaluable help with the TC4 dataset and Gerry Heymsfield for providing the ER-2 radar data from TC4. This research was supported by the National Aeronautics and Space Administration (NASA) through Award (GPM) NNX13AH73G, and from the NASA Jet Propulsion Laboratory, California Institute of Technology (JPL), with Deb Vane as contract monitor. Work by NBW was performed at the University of Wisconsin–Madison for JPL, sponsored by NASA. Assistance from Meg Miller for her technical editing of the document was invaluable.

REFERENCES

Bohren, C. F., and D. R. Huffman, 1983: *Absorption and Scattering of Light by Small Particles*. John Wiley and Sons, 530 pp.

Boucher, R. J., and J. G. Wieler, 1985: Radar determination of snowfall rate and accumulation. *J. Climate Appl. Meteor.*, **24**, 68–73, doi:10.1175/1520-0450(1985)024<0068:RDOSRA>2.0.CO;2.

Braham, R. R., Jr., 1990: Snow particle size spectra in lake effect snow. *J. Appl. Meteor.*, **29**, 200–207, doi:10.1175/1520-0450(1990)029<0200:SPSSIL>2.0.CO;2.

Brown, P. R. A., and P. N. Francis, 1995: Improved measurements of the ice water content in cirrus using a total-water probe. *J. Atmos. Oceanic Technol.*, **12**, 410–414, doi:10.1175/1520-0426(1995)012<0410:IMOTIW>2.0.CO;2.

Deng, M., G. G. Mace, Z. Wang, and H. Okamoto, 2010: Tropical Composition, Cloud and Climate Coupling Experiment validation for cirrus cloud profiling retrieval using *CloudSat* radar and *CALIPSO* lidar. *J. Geophys. Res.*, **115**, D00J15, doi:10.1029/2009JD013104.

——, ——, ——, and R. P. Lawson, 2013: Evaluation of several A-Train ice cloud retrieval products with in situ measurements collected during the SPARTICUS campaign. *J. Appl. Meteor. Climatol.*, **52**, 1014–1030, doi:10.1175/JAMC-D-12-054.1.

Field, P. R., A. J. Heymsfield, and A. Bansemer, 2006: Shattering and particle interarrival times measured by optical array probes in ice clouds. *J. Atmos. Oceanic Technol.*, **23**, 1357–1371, doi:10.1175/JTECH1922.1.

Fujiyoshi, Y., T. Endoh, T. Yamada, K. Tsuboki, Y. Tachibana, and G. Wakahama, 1990: Determination of a *Z–R* relationship for snowfall using a radar and high sensitivity snow gauges. *J. Appl. Meteor.*, **29**, 147–152, doi:10.1175/1520-0450(1990)029<0147:DOARFS>2.0.CO;2.

Gaussiat, N., H. Sauvageot, and A. J. Illingworth, 2003: Cloud liquid water and ice content retrieval by multiwavelength radar. *J. Atmos. Oceanic Technol.*, **20**, 1264–1275, doi:10.1175/1520-0426(2003)020<1264:CLWAIC>2.0.CO;2.

Hammonds, K. D., G. G. Mace, and S. Y. Matrosov, 2014: Characterizing the radar backscatter-cross-section sensitivities of ice-phase hydrometeor size distributions via a simple scaling of the Clausius–Mossotti factor. *J. Appl. Meteor. Climatol.*, **53**, 2761–2774, doi:10.1175/JAMC-D-13-0280.1.

Hanesch, M., 1999: Fall velocity and shape of snowflakes. Ph.D. thesis, Swiss Federal Institute of Technology, Zurich, Switzerland, 123 pp. [Available online at http://e-collection.library.ethz.ch/eserv/eth:23207/eth-23207-02.pdf.]

Haynes, J. M., T. S. L'Ecuyer, G. L. Stephens, S. D. Miller, C. Mitrescu, N. B. Wood, and S. Tanelli, 2009: Rainfall retrieval over the ocean with spaceborne W-band radar. *J. Geophys. Res.*, **114**, D00A22, doi:10.1029/2008JD009973.

Heymsfield, A. J., and J. L. Parrish, 1978: A computational technique for increasing the effective sampling volume of the PMS two-dimensional particle size spectrometer. *J. Appl. Meteor.*, **17**, 1566–1572, doi:10.1175/1520-0450(1978)017<1566:ACTFIT>2.0.CO;2.

——, and A. G. Palmer, 1986: Relationships for deriving thunderstorm anvil mass flux for CCOPE storm water budget estimates. *J. Climate Appl. Meteor.*, **25**, 691–702, doi:10.1175/1520-0450(1986)025<0691:RFDTAI>2.0.CO;2.

——, and C. D. Westbrook, 2010: Advances in the estimation of ice particle fall speeds using laboratory and field measurements. *J. Atmos. Sci.*, **67**, 2469–2482, doi:10.1175/2010JAS3379.1.

——, A. Bansemer, P. R. Field, S. L. Durden, J. Stith, J. E. Dye, and W. Hall, 2002: Observations and parameterizations of particle size distributions in deep tropical cirrus and stratiform precipitating clouds: Results from in situ observations in TRMM field campaigns. *J. Atmos. Sci.*, **59**, 3457–3491, doi:10.1175/1520-0469(2002)059<3457:OAPOPS>2.0.CO;2.

——, ——, C. Schmitt, C. Twohy, and M. Poellot, 2004: Effective ice particle densities derived from aircraft data. *J. Atmos. Sci.*, **61**, 982–1003, doi:10.1175/1520-0469(2004)061<0982:EIPDDF>2.0.CO;2.

——, Z. Wang, and S. Matrosov, 2005: Improved radar ice water content retrieval algorithms using coincident microphysical and radar measurements. *J. Appl. Meteor.*, **44**, 1391–1412, doi:10.1175/JAM2282.1.

——, C. Schmitt, and A. Bansemer, 2013: Ice cloud particle size distributions and pressure-dependent terminal velocities from in situ observations at temperatures from 0° to −86°C. *J. Atmos. Sci.*, **70**, 4123–4154, doi:10.1175/JAS-D-12-0124.1.

——, A. Bansemer, M. R. Poellot, and N. Wood, 2015: Observations of ice microphysics through the melting layer. *J. Atmos. Sci.*, **72**, 2902–2928, doi:10.1175/JAS-D-14-0363.1.

Heymsfield, G. M., L. Tian, A. J. Heymsfield, L. Li, and S. Guimond, 2010: Characteristics of deep tropical and subtropical convection from nadir-viewing high-altitude airborne Doppler radar. *J. Atmos. Sci.*, **67**, 285–308, doi:10.1175/2009JAS3132.1.

Hiley, M. J., M. S. Kulie, and R. Bennartz, 2011: Uncertainty analysis for *CloudSat* snowfall retrievals. *J. Appl. Meteor. Climatol.*, **50**, 399–418, doi:10.1175/2010JAMC2505.1.

Hogan, R. J., and C. D. Westbrook, 2014: Equation for the microwave backscatter cross section of aggregate snowflakes using the self-similar Rayleigh–Gans approximation. *J. Atmos. Sci.*, **71**, 3292–3301, doi:10.1175/JAS-D-13-0347.1.

——, M. P. Mittermaier, and A. J. Illingworth, 2006: The retrieval of ice water content from radar reflectivity factor and temperature and its use in evaluating a mesoscale model. *J. Appl. Meteor. Climatol.*, **45**, 301–317, doi:10.1175/JAM2340.1.

Hong, G., 2007: Radar backscattering properties of nonspherical ice crystals at 94 GHz. *J. Geophys. Res.*, **112**, D22203, doi:10.1029/2007JD008839.

Huang, G. W., V. N. Bringi, D. Moisseev, W. A. Petersen, L. Bliven, and D. Hudak, 2015: Use of 2D-video disdrometer to derive mean density–size and Z_e–SR relations: Four snow cases from the Light Precipitation Validation Experiment. *Atmos. Res.*, **153**, 34–48, doi:10.1016/j.atmosres.2014.07.013.

Imai, I., M. Fujiwara, I. Chimura, and Y. Toyama, 1955: Radar reflectivity of falling snow. *Pap. Meteor. Geophys.*, **6**, 130–139.

Intrieri, J. M., G. L. Stephens, W. L. Eberhard, and T. Uttal, 1993: A method for determining cirrus cloud particle sizes using lidar and radar backscatter technique. *J. Appl. Meteor.*, **32**, 1074–1082, doi:10.1175/1520-0450(1993)032<1074:AMFDCC>2.0.CO;2.

King, W. D., 1986: Air flow and particle trajectories around aircraft fuselages. IV: Orientation of ice crystals. *J. Atmos. Oceanic Technol.*, **3**, 433–439, doi:10.1175/1520-0426(1986)003<0433:AFAPTA>2.0.CO;2.

Korolev, A., and G. Isaac, 2003: Roundness and aspect ratio of particles in ice clouds. *J. Atmos. Sci.*, **60**, 1795–1808, doi:10.1175/1520-0469(2003)060<1795:RAAROP>2.0.CO;2.

Kulie, M. S., and R. Bennartz, 2009: Utilizing spaceborne radars to retrieve dry snowfall. *J. Appl. Meteor. Climatol.*, **48**, 2564–2580, doi:10.1175/2009JAMC2193.1.

——, ——, T. J. Greenwald, Y. Chen, and F. Weng, 2010: Uncertainties in microwave properties of frozen precipitation: Implications for remote sensing and data assimilation. *J. Atmos. Sci.*, **67**, 3471–3487, doi:10.1175/2010JAS3520.1.

Lebsock, M. D., and T. S. L'Ecuyer, 2011: The retrieval of warm rain from *CloudSat*. *J. Geophys. Res.*, **116**, D20209, doi:10.1029/2011JD016076.

Leinonen, J., S. Kneifel, D. Moisseev, J. Tyynela, S. Tanelli, and T. Nousiainen, 2012: Nonspheroidal behavior in millimeter-wavelength radar observations of snowfall. *J. Geophys. Res.*, **117**, D18205, doi:10.1029/2012JD017680.

Liao, L., R. Meneghini, L. Tian, and G. Heymsfield, 2008: Retrieval of snow and rain from combined X- and W-band airborne

radar measurements. *IEEE Trans. Geosci. Remote Sens.*, **46**, 1514–1524, doi:10.1109/TGRS.2008.916079.

Liu, C. L., and A. J. Illingworth, 2000: Toward more accurate retrievals of ice water content from radar measurements of clouds. *J. Appl. Meteor.*, **39**, 1130–1146, doi:10.1175/1520-0450(2000)039<1130:TMAROI>2.0.CO;2.

Liu, G., 2008: Deriving snow cloud characteristics from *CloudSat* observations. *J. Geophys. Res.*, **113**, D00A09, doi:10.1029/2007JD009766.

Marshall, J. S., and W. M. Palmer, 1948: The distribution of raindrops with size. *J. Meteor.*, **5**, 165–166, doi:10.1175/1520-0469(1948)005<0165:TDORWS>2.0.CO;2.

Matrosov, S. Y., 1992: Radar reflectivity in snowfall. *IEEE Trans. Geosci. Remote Sens.*, **30**, 454–461, doi:10.1109/36.142923.

——, 1997: Variability of microphysical parameters in high-altitude ice clouds: Results of the remote sensing method. *J. Appl. Meteor.*, **36**, 633–648, doi:10.1175/1520-0450-36.6.633.

——, 1998: A dual-wavelength radar method to measure snowfall rate. *J. Appl. Meteor.*, **37**, 1510–1521, doi:10.1175/1520-0450(1998)037<1510:ADWRMT>2.0.CO;2.

——, 2007: Modeling backscatter properties of snowfall at millimeter wavelengths. *J. Atmos. Sci.*, **64**, 1727–1736, doi:10.1175/JAS3904.1.

——, and A. J. Heymsfield, 2008: Estimating ice content and extinction in precipitating cloud systems from *CloudSat* radar measurements. *J. Geophys. Res.*, **113**, D00A05, doi:10.1029/2007JD009633.

——, B. W. Orr, R. A. Kropfli, and J. B. Snider, 1994: Retrieval of vertical profiles of cirrus cloud microphysical parameters from Doppler radar and infrared radiometer measurements. *J. Appl. Meteor.*, **33**, 617–626, doi:10.1175/1520-0450(1994)033<0617:ROVPOC>2.0.CO;2.

——, C. Campbell, D. Kingsmill, and E. Sukovich, 2009: Assessing snowfall rates from X-band radar reflectivity measurements. *J. Atmos. Oceanic Technol.*, **26**, 2324–2339, doi:10.1175/2009JTECHA1238.1.

McGill, M. J., D. L. Hlavka, W. D. Hart, E. J. Welton, and J. R. Campbell, 2003: Airborne lidar measurements of aerosol optical properties during SAFARI-2000. *J. Geophys. Res.*, **108**, 8493, doi:10.1029/2002JD002370.

Mitchell, D. L., and A. J. Heymsfield, 2005: Refinements in the treatment of ice particle terminal velocities, highlighting aggregates. *J. Atmos. Sci.*, **62**, 1637–1644, doi:10.1175/JAS3413.1.

Mitrescu, C., T. L'Ecuyer, J. Haynes, S. Miller, and J. Turk, 2010: *CloudSat* precipitation profiling algorithm-model description. *J. Appl. Meteor. Climatol.*, **49**, 991–1003, doi:10.1175/2009JAMC2181.1.

Ohtake, T., 1970: Factors affecting the size distribution of raindrops and snowflakes. *J. Atmos. Sci.*, **27**, 804–813, doi:10.1175/1520-0469(1970)027<0804:FATSDO>2.0.CO;2.

Petty, G. W., and W. Huang, 2010: Microwave backscatter and extinction by soft ice spheres and complex snow aggregates. *J. Atmos. Sci.*, **67**, 769–787, doi:10.1175/2009JAS3146.1.

Protat, A., J. Delanoë, D. Bouniol, A. J. Heymsfield, A. Bansemer, and P. Brown, 2007: Evaluation of ice water content retrievals from cloud radar reflectivity and temperature using a large airborne in situ microphysical database. *J. Appl. Meteor. Climatol.*, **46**, 557–572, doi:10.1175/JAM2488.1.

Puhakka, T., 1975: On the dependence of *Z–R* relation on the temperature in snowfall. Preprints, *16th Radar Meteorology Conf.*, Houston, TX, Amer. Meteor. Soc., 504–507.

Rasmussen, R., M. Dixon, S. Vasiloff, F. Hage, S. Knight, J. Vivekanandan, and M. Xu, 2003: Snow nowcasting using a real-time correlation of radar reflectivity with snow gauge accumulation. *J. Appl. Meteor.*, **42**, 20–36, doi:10.1175/1520-0450(2003)042<0020:SNUART>2.0.CO;2.

Rodgers, C. D., 2000: *Inverse Methods for Atmospheric Sounding: Theory and Practice*. World Scientific Publishing, 240 pp.

Sekelsky, S. M., W. L. Ecklund, J. M. Firda, K. S. Gage, and R. E. McIntosh, 1999: Particle size estimation in ice-phase clouds using multifrequency radar reflectivity measurements at 95, 33, and 2.8 GHz. *J. Appl. Meteor.*, **38**, 5–28, doi:10.1175/1520-0450(1999)038<0005:PSEIIP>2.0.CO;2.

Sekhon, R. S., and R. C. Srivastava, 1970: Snow size spectra and radar reflectivity. *J. Atmos. Sci.*, **27**, 299–307, doi:10.1175/1520-0469(1970)027<0299:SSSARR>2.0.CO;2.

Surussavadee, C., and D. H. Staelin, 2006: Comparison of AMSU millimeter-wave satellite observations, MM5/TBSCAT predicted radiances, and electromagnetic models for hydrometeors. *IEEE Trans. Geosci. Remote Sens.*, **44**, 2667–2678, doi:10.1109/TGRS.2006.873275.

Tinel, C., J. Testud, J. Pelon, R. H. Hogan, A. Protat, J. Delanoë, and D. Bouniol, 2005: The retrieval of ice cloud properties from cloud radar and lidar synergy. *J. Appl. Meteor.*, **44**, 860–875, doi:10.1175/JAM2229.1.

Toon, O. B., and Coauthors, 2010: Planning, implementation, and first results of the Tropical Composition, Cloud and Climate Coupling Experiment (TC4). *J. Geophys. Res.*, **115**, D00J04, doi:10.1029/2009JD013073.

Twohy, C. H., A. J. Schanot, and W. A. Cooper, 1997: Measurement of condensed water content in liquid and ice clouds using an airborne counterflow virtual impactor. *J. Atmos. Oceanic Technol.*, **14**, 197–202, doi:10.1175/1520-0426(1997)014<0197:MOCWCI>2.0.CO;2.

Tyynela, J., J. Leinonen, D. Moisseev, and T. Nousiainen, 2011: Radar backscattering from snowflakes: Comparison of fractal, aggregate, and soft-spheroid models. *J. Atmos. Oceanic Technol.*, **28**, 1365–1372, doi:10.1175/JTECH-D-11-00004.1.

Vasiloff, S., P. Bukovcic, A. Arthur, M. P. Meyers, K. Houck, J. Busto, and L. Tang, 2013: Evaluation of snowfall estimates from the Grand Junction, Colorado WSR-88D during winter 2012-2013. *Proc. 36th Conf. on Radar Meteorology*, Breckenridge, CO, Amer. Meteor. Soc., 14B.4. [Available online at https://ams.confex.com/ams/36Radar/webprogram/Paper228534.html.]

Wang, Z., and K. Sassen, 2002: Cirrus cloud microphysical property retrieval using lidar and radar measurements. Part I: Algorithm description and comparison with in situ data. *J. Appl. Meteor.*, **41**, 218–229, doi:10.1175/1520-0450(2002)041<0218:CCMPRU>2.0.CO;2.

——, G. M. Heymsfield, L. Li, and A. J. Heymsfield, 2005: Retrieving optically thick ice cloud microphysical properties by using airborne dual-wavelength radar measurements. *J. Geophys. Res.*, **110**, D19201, doi:10.1029/2005JD005969.

Wolfe, J. P., and J. R. Snider, 2012: A relationship between reflectivity and snow rate for a high-altitude S-band radar. *J. Appl. Meteor. Climatol.*, **51**, 1111–1128, doi:10.1175/JAMC-D-11-0112.1.

Wood, N. B., T. S. L'Ecuyer, A. J. Heymsfield, and G. L. Stephens, 2015: Microphysical constraints on millimeter-wavelength scattering properties of snow particles. *J. Appl. Meteor. Climatol.*, **54**, 909–931, doi:10.1175/JAMC-D-14-0137.1.